INTERNATIONAL JOURNAL FOR NUMERICAL AND ANALYTICAL METHODS IN GEOMECHANICS
Int. J. Numer. Anal. Meth. Geomech. 2012; **36**:1535–1573
Published online 18 August 2011 in Wiley Online Library (wileyonlinelibrary.com). DOI: 10.1002/nag.1061

Dynamics of unsaturated poroelastic solids at finite strain

Ryosuke Uzuoka[1,*,†] and Ronaldo I. Borja[2]

[1]*Department of Civil and Environmental Engineering, The University of Tokushima, Minamijyousanjima 2–1, Tokushima, 770–8506, Japan*
[2]*Department of Civil and Environmental Engineering, Stanford University, Stanford, CA 94305–4020, USA*

SUMMARY

We derive the governing equations for the dynamic response of unsaturated poroelastic solids at finite strain. We obtain simplified governing equations from the complete coupled formulation by neglecting the material time derivative of the relative velocities and the advection terms of the pore fluids relative to the solid skeleton, leading to a so-called $u^{\mathrm{s}}-p^{\mathrm{w}}-p^{\mathrm{a}}$ formulation. We impose the weak forms of the momentum and mass balance equations at the current configuration and implement the framework numerically using a mixed finite element formulation. We verify the proposed method through comparison with analytical solutions and experiments of quasi-static processes. We use a neo-Hookean hyperelastic constitutive model for the solid matrix and demonstrate, through numerical examples, the impact of large deformation on the dynamic response of unsaturated poroelastic solids under a variety of loading conditions. Copyright © 2011 John Wiley & Sons, Ltd.

Received 12 November 2009; Revised 6 May 2011; Accepted 8 May 2011

KEY WORDS: unsaturated media; porous media; finite strain; finite element method

1. INTRODUCTION

In 1972, Biot [1] brought the mechanics of porous media to the same level of development as the classical theory of finite deformations in elasticity. In his formulation, he considered the solid motion as a continuous sequence of incremental deformations. Because the solid properties are transported and rotated with the motion, he used a Lagrangian or material description of deformation, in contrast to the Eulerian or spatial description that is more appropriate for isotropic homogeneous fluids. Since then, a number of finite deformation theories for porous solids utilizing a Lagrangian formulation have emerged in the literature. However, a majority of them have focused solely on quasi-static deformations [2–7]. In 2004, Li and Borja [8] formulated a completely Lagrangian description of the dynamics of fully saturated poroelastic solids. They used a neo-Hookean hyperelasticity enhanced with a Kelvin-type viscosity for the solid matrix and implemented the formulation within the framework of mixed finite elements. Their work has focused on the effect of large deformation on the dynamic response of fully saturated poroelastic material. The present paper takes one step further and aims to incorporate partial saturation into the formulation.

The complex interplay among solid deformation, fluid diffusion, partial saturation, and large deformation in a dynamic setting can be addressed in a coherent manner by using porous media theory combined with today's most advanced computational tools [9]. Porous media theory has been used

*Correspondence to: Ryosuke Uzuoka, Department of Civil and Environmental Engineering, The University of Tokushima, Minamijyousanjima 2–1, Tokushima, 770–8506 Japan.
†E-mail: uzuoka@ce.tokushima-u.ac.jp

by several researchers since the 1980s [10–24]. Applications to more complicated problems of 3D soil-structure interaction have been proposed in [25–30]. Dynamic coupled analysis at finite strain has also been proposed in [8, 31]. Coupled analyses of unsaturated soil response have been presented in [31, 32] using the degree of saturation as a prime variable, without determining the pore air pressure explicitly. However, the compressibility of the pore air plays an important role in the dynamic response of unsaturated soil [33] and hence should be considered in the formulation of boundary-value problems. Recently, pore air pressure has been treated as a primary variable in [34–36]; however, their numerical applications are limited to the regime of small deformation.

In this paper, we use the porous media theory for the problem of coupled solid deformation-fluid flow processes for unsaturated poroelastic materials. The contribution of the paper lies on the insight gained into the effect of finite deformation on the static and dynamic responses of unsaturated porous media under complex loading and displacement boundary conditions for which a numerical solution is most appropriate. In order not to obscure the effect of finite deformation by the nonlinearity in material response, including the plastic hysteretic response from cyclic loading, we limit the scope of this paper to a solid matrix characterized by a neo-Hookean hyperelastic material. However, the constitutive formulation is still based on the use of a thermodynamically consistent 'effective stress' measure for the solid matrix response [37, 38] and can be readily extended to the elastoplastic regime.

The paper begins with a complete formulation for the momentum and mass conservation equations, which then paves the way for the simplified formulation that is used in the numerical implementation. In the simplified formulation, we neglect the material time derivatives of relative velocities and the advection terms of the pore fluids with respect to the solid matrix, leading to a so-called $u^{\mathrm{s}} - p^{\mathrm{w}} - p^{\mathrm{a}}$ formulation. The weak forms of the momentum and mass balance equations are implemented in a finite element framework by imposing the conservation laws in the current configuration. The matrix equations are then linearized consistently and solved by Newton-Raphson iteration. We conclude the paper with some numerical examples aimed at demonstrating the impact of finite deformation on the mechanical response of unsaturated poroelastic systems, as well as the efficacy of the proposed nonlinear iterative algorithm.

2. GOVERNING EQUATIONS AT FINITE STRAIN

Following the porous media theory for a solid-water-air mixture at finite strain [39, 40], the kinematics of motions of the solid skeleton is described with Lagrangian coordinates, while those of pore water and air are described with Eulerian coordinates with respect to the current configuration of the solid skeleton.

First, we introduce the basic equations including balance laws and constitutive equations. Second, we combine the basic equations and constitutive equations to obtain the full formulation of the boundary-value problem. Finally, we derive the simplified governing equations in terms of the solid skeleton displacement $\boldsymbol{u}^s$, pore water pressure p^w, and pore air pressure p^a as the primary variables. The simplified governing equations consist of the momentum balance equations for the overall three-phase mixture and the mass and momentum balance equations for the pore water and air.

2.1. Basic assumptions

Porous media theory is based on a representation of two or more species occupying the same space at the same time. The theory relies on the notion of volume fractions and is depicted pictorially in Figure 1 in the context of a three-phase solid-water-air mixture.

The kinematics of each phase is based on the following assumptions [39]:

- The spatial point occupied by each material $\boldsymbol{X}^\alpha$ in the current configuration is the common point $\boldsymbol{x}$.
- At the common spatial point $\boldsymbol{x}$, the motions of the individual phases define the interaction among these phases.

In the above definition, the superscript α means a phase, "s" means solid skeleton, "w" means pore water, and "a" means pore air. In addition, we make the following simplifying assumptions:

1. isothermal conditions,
2. incompressible solid particle,

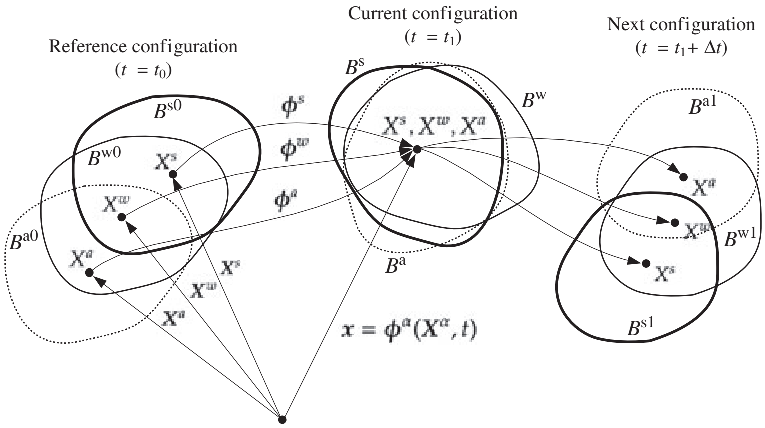

Figure 1. Kinematics of a three-phase porous continuum.

3. no mass exchange between the solid and fluid constituents,
4. the material time derivatives of relative velocity of the pore fluids to the solid skeleton are small compared to the acceleration of the solid skeleton, and
5. the advection terms of the pore fluids to the solid skeleton are small as compared to the acceleration of the solid skeleton.

Assumption 3 means that the solid and fluid are immiscible, but it does not rule out the exchange of mass between water and air. In general, pore air dissolves into pore water following Henry's law. The dissolution of pore air affects pore fluid compressibility and the pore fluid responses of unsaturated soil during shear loading [41, 42]. Their implementation may require more complex equations of state [43] that are not covered in the present paper.

2.2. *Volume fraction and partial density*

The volume fraction $n^\alpha(\boldsymbol{x}, t)$ of a phase α is defined as

$$n^\alpha(\boldsymbol{x}, t) = \frac{dv^\alpha}{dv}, \tag{1}$$

where dv^α is the volume of α phase in the current configuration, and dv is the overall volume of porous media. The partial density of each phase is defined as the averaged density with the volume fraction n^α as

$$\rho^{\mathrm{s}} = n^{\mathrm{s}}\rho^{\mathrm{sR}} = (1-n)\rho^{\mathrm{sR}}, \tag{2}$$

$$\rho^{\mathrm{w}} = n^{\mathrm{w}}\rho^{\mathrm{wR}} = ns^{\mathrm{w}}\rho^{\mathrm{wR}}, \tag{3}$$

$$\rho^{\mathrm{a}} = n^{\mathrm{a}}\rho^{\mathrm{aR}} = ns^{\mathrm{a}}\rho^{\mathrm{aR}} = n(1-s^{\mathrm{w}})\rho^{\mathrm{aR}}, \tag{4}$$

where ρ^{sR}, ρ^{wR}, and ρ^{aR} are the intrinsic density of solid skeleton, pore water, and pore air, respectively. n^{s}, n^{w}, and n^{a} are the volume fraction of solid skeleton, pore water, and pore air, respectively, in the current configuration. n, s^{w}, and s^{a} are the porosity, degree of water saturation, and degree of air saturation, respectively, in the current configuration. The overall density of mixture ρ can be expressed as

$$\rho = \rho^{\mathrm{s}} + \rho^{\mathrm{w}} + \rho^{\mathrm{a}} = (1-n)\rho^{\mathrm{sR}} + n\left(s^{\mathrm{w}}\rho^{\mathrm{wR}} + s^{\mathrm{a}}\rho^{\mathrm{aR}}\right). \tag{5}$$

2.3. Kinematics of porous media

The spatial description x of the material point X^α is given as

$$\boldsymbol{x} = \varphi^\alpha(\mathrm{X}^\alpha, t), \tag{6}$$

where φ^α denotes the motion of the material point $\boldsymbol{X}^\alpha$ in Figure 1. The velocity $\boldsymbol{v}^\alpha$ of the material point $\boldsymbol{X}^\alpha$ is defined as the time derivative of φ^α:

$$\boldsymbol{v}^\alpha = \frac{\partial x}{\partial t} = \frac{\partial \varphi^\alpha(\boldsymbol{X}^\alpha, t)}{\partial t}. \tag{7}$$

The acceleration of solid skeleton $\boldsymbol{a}^\mathrm{s}$ is given by the material time derivative $D^s\square/Dt$ with respect to solid skeleton as

$$\boldsymbol{a}^\mathrm{s} = \frac{D^\mathrm{s}\boldsymbol{v}^\mathrm{s}}{Dt} = \frac{\partial \boldsymbol{v}^\mathrm{s}}{\partial t} + (\mathrm{grad}\ \boldsymbol{v}^\mathrm{s})\boldsymbol{v}^\mathrm{s}, \tag{8}$$

where $\boldsymbol{v}^\mathrm{s}$ is the velocity of solid skeleton. The acceleration of pore water $\boldsymbol{a}^\mathrm{w}$ can be expressed in terms of the material time derivative $D^s\square/Dt$ as

$$\boldsymbol{a}^\mathrm{w} = \frac{D^\mathrm{w}\boldsymbol{v}^\mathrm{w}}{Dt} = \boldsymbol{a}^\mathrm{s} + \frac{D^\mathrm{s}\boldsymbol{v}^\mathrm{ws}}{Dt} + \{\mathrm{grad}\ (\boldsymbol{v}^\mathrm{s} + \boldsymbol{v}^\mathrm{ws})\}\boldsymbol{v}^\mathrm{ws}, \tag{9}$$

where $\boldsymbol{v}^\mathrm{ws}$ is the relative velocity of pore water to the solid skeleton. Similarly, the acceleration of pore air $\boldsymbol{a}^\mathrm{a}$ also can be expressed with the relative velocity $\boldsymbol{v}^\mathrm{as}$ as

$$\boldsymbol{a}^\mathrm{a} = \frac{D^\mathrm{a}\boldsymbol{v}^\mathrm{a}}{Dt} = \boldsymbol{a}^\mathrm{s} + \frac{D^\mathrm{s}\boldsymbol{v}^\mathrm{as}}{Dt} + \{\mathrm{grad}\ (\boldsymbol{v}^\mathrm{s} + \boldsymbol{v}^\mathrm{as})\}\boldsymbol{v}^\mathrm{as}. \tag{10}$$

The motions of pore fluids including water and air are described with reference to the solid skeleton configuration.

2.4. Balance laws

The mass balance law for phase α in the current configuration may be written as

$$\frac{D^\alpha\rho^\alpha}{Dt} + \rho^\alpha\ \mathrm{div}\ \boldsymbol{v}^\alpha = m^\alpha, \tag{11}$$

where m^α is the mass exchange term for phase α. Assuming the solid and fluid do not exchange mass, then $m^\mathrm{s} = 0$, in which case, the exchange of mass can only take place between water and air. Because the entire mixture cannot produce mass, it follows that $m^\mathrm{w} + m^\mathrm{a} = 0$. This is called the summing rule or the closure condition. The momentum balance law for phase α in the current configuration is

$$\rho^\alpha\boldsymbol{a}^\alpha + m^\alpha\boldsymbol{v}^\alpha = \mathrm{div}\ \boldsymbol{\sigma}^\alpha + \rho^\alpha\boldsymbol{b}^\alpha + \hat{\boldsymbol{p}}^\alpha, \tag{12}$$

where $\boldsymbol{\sigma}^\alpha$ is the averaged Cauchy stress tensor of phase α, $\boldsymbol{b}^\alpha$ is the gravity acceleration vector for phase α, and $\hat{\boldsymbol{p}}^\alpha$ is the interaction force vector between phase α and other phases. The interaction force vectors $\hat{\boldsymbol{p}}^\alpha$ also satisfy the summing rule, $\sum_{\alpha=1}^{3}\hat{\boldsymbol{p}}^\alpha = \boldsymbol{0}$. In general, the mass exchange terms depend on the properties and thermodynamic states of the constituents. Because the focus of the paper is the hydro-mechanical response under large deformation, we will not consider this term in the following development. We note, however, that mass exchanges could play an important role in high-frequency dynamical processes, such as soil blasting.

2.5. Constitutive equations

From thermodynamic studies [37, 38, 44–50] on the effective stress of unsaturated soil, we use a consistent 'effective stress' measure for the solid matrix response. For partially saturated porous continua, the general expression for the Cauchy effective stress tensor $\boldsymbol{\sigma}'$ consistent with continuum principles of thermodynamics is [37]

$$\boldsymbol{\sigma}' = \boldsymbol{\sigma} + B\,\overline{p}\boldsymbol{I}, \tag{13}$$

where $\boldsymbol{\sigma}$ is the total Cauchy stress tensor, B is the Biot coefficient, $\boldsymbol{I}$ is the second-order identity tensor (Kronecker delta function), and $\overline{p}$ is the mean pore pressure given by the expression:

$$\overline{p} = s^{\mathrm{w}} p^{\mathrm{w}} + s^{\mathrm{a}} p^{\mathrm{a}}, \tag{14}$$

where p^{w} and p^{a} are the pore water and pore air pressures, respectively. This definition for effective stress may be readily extended to double porosity continua [38]. Furthermore, the above expression for the effective stress readily specializes to more familiar forms, including the Bishop stress [51] when $B=1$ and $s^{\mathrm{w}}=\chi$ (where χ is the Bishop parameter) and the Terzaghi stress [52] when $B=1$, $s^{\mathrm{a}}=0$ and $s^{\mathrm{w}}=1$. For soils, the Biot coefficient B may be taken as equal to one, and so, an equivalent effective stress equation may be written in the form:

$$\boldsymbol{\sigma} = \boldsymbol{\sigma}' - p^{\mathrm{a}}\boldsymbol{I} + s^{\mathrm{w}} p^{\mathrm{c}}\boldsymbol{I}, \tag{15}$$

where $p^{\mathrm{c}}=(p^{\mathrm{a}}-p^{\mathrm{w}})$ is the suction stress or capillary pressure. In the above expression for the total Cauchy stress tensor, we have utilized the closure condition $s^{\mathrm{a}}+s^{\mathrm{w}}=1$. Using the equivalent effective stress, the averaged (or partial) Cauchy stress tensor for each phase may be written as

$$\boldsymbol{\sigma}^{\mathrm{s}} = \boldsymbol{\sigma}' - (1-n)\overline{p}\boldsymbol{I}, \tag{16}$$

$$\boldsymbol{\sigma}^{\mathrm{w}} = -n s^{\mathrm{w}} p^{\mathrm{w}}\boldsymbol{I}, \tag{17}$$

$$\boldsymbol{\sigma}^{\mathrm{a}} = -n s^{\mathrm{a}} p^{\mathrm{a}}\boldsymbol{I}, \tag{18}$$

where $\boldsymbol{\sigma}^{\mathrm{s}}$, $\boldsymbol{\sigma}^{\mathrm{w}}$, and $\boldsymbol{\sigma}^{\mathrm{a}}$ are the averaged Cauchy stress tensors for the solid skeleton, pore water, and pore air, respectively.

Interaction forces between fluid phases and solid skeleton are also derived based on thermodynamic studies [39, 40, 44, 45] as

$$\hat{\boldsymbol{p}}^{\alpha} = p^{\alpha}\,\mathrm{grad}\; n^{\alpha} - \boldsymbol{\mu}^{\alpha} n^{\alpha}\boldsymbol{v}^{\alpha s}, \tag{19}$$

where μ^{α} is the material parameter tensor. The interaction forces for three phases are

$$\hat{\boldsymbol{p}}^{\mathrm{s}} = -\hat{\boldsymbol{p}}^{\mathrm{w}} - \hat{\boldsymbol{p}}^{\mathrm{a}}, \tag{20}$$

$$\hat{\boldsymbol{p}}^{\mathrm{w}} = p^{\mathrm{w}}\;\mathrm{grad}\,(n s^{\mathrm{w}}) - \boldsymbol{\mu}^{\mathrm{w}} n s^{\mathrm{w}}\boldsymbol{v}^{\mathrm{ws}}, \tag{21}$$

$$\hat{\boldsymbol{p}}^{\mathrm{a}} = p^{\mathrm{a}}\;\mathrm{grad}\,(n s^{\mathrm{a}}) - \boldsymbol{\mu}^{\mathrm{a}} n s^{\mathrm{a}}\boldsymbol{v}^{\mathrm{as}}. \tag{22}$$

Assuming that the permeability coefficients k^{ws} of pore water and k^{as} of pore air are isotropic, the material parameter tensors $\boldsymbol{\mu}^{\alpha}$ can be expressed as

DOI: 10.1002/nag

$$\boldsymbol{\mu}^{\mathrm{w}} = \frac{ns^{\mathrm{w}}\rho^{\mathrm{wR}}g}{k^{\mathrm{ws}}}\boldsymbol{I}, \tag{23}$$

$$\boldsymbol{\mu}^{\mathrm{a}} = \frac{ns^{\mathrm{a}}\rho^{\mathrm{aR}}g}{k^{\mathrm{as}}}\boldsymbol{I}, \tag{24}$$

where g is the gravity acceleration.

The state equation for the pore water that leads to the constitutive law for the compressibility of pore water can be obtained with Assumption 1 and the material time derivative with respect to the solid skeleton as

$$\frac{D^{\mathrm{s}}\rho^{\mathrm{wR}}}{Dt} = \frac{\rho^{\mathrm{wR}}}{K^{\mathrm{w}}}\frac{D^{\mathrm{s}}p^{\mathrm{w}}}{Dt}, \tag{25}$$

where K^{w} is the bulk modulus of pore water. Similarly, the constitutive law for the compressibility of pore air is given by

$$\frac{D^{\mathrm{s}}p^{\mathrm{a}}}{Dt} = \Theta\bar{R}\frac{D^{\mathrm{s}}\rho^{\mathrm{aR}}}{Dt}, \tag{26}$$

where Θ is the absolute temperature, and $\bar{R}$ is the specific gas constant of air.

The material time derivative of water saturation s^{w} with respect to the solid skeleton can be expressed in terms of the matric suction p^{c}:

$$\frac{D^{\mathrm{s}}s^{\mathrm{w}}}{Dt} = \frac{\partial s^{\mathrm{w}}}{\partial p^{\mathrm{c}}}\frac{D^{\mathrm{s}}p^{\mathrm{c}}}{Dt} = c\frac{D^{\mathrm{s}}p^{\mathrm{c}}}{Dt}, \tag{27}$$

where c is the specific moisture capacity defined by the soil-water characteristics curve (SWCC) in Figure 2. Two SWCC models are used in this study. The first is a popular empirical SWCC model (VG model) proposed by van Genuchten [53], whereas the second is a logistic SWCC model (LG model) similar to that presented in [54]. We remark that both models are empirical, as are nearly all other SWCC models available in literature. As such, the model parameters are determined from curve-fitting with experimentally determined water retention curves.

In the VG model,

$$s_{\mathrm{e}}^{\mathrm{w}} = \left\{1 + \left(\alpha_{\mathrm{vg}}p^{\mathrm{c}}\right)^{n_{\mathrm{vg}}}\right\}^{-m_{\mathrm{vg}}}, \tag{28}$$

where $s_{\mathrm{e}}^{\mathrm{w}}$ is the effective degree of water saturation, and α_{vg}, n_{vg}, and m_{vg} are the material parameters of VG model. The effective degree of water saturation $s_{\mathrm{e}}^{\mathrm{w}}$ in Figure 2 is defined as

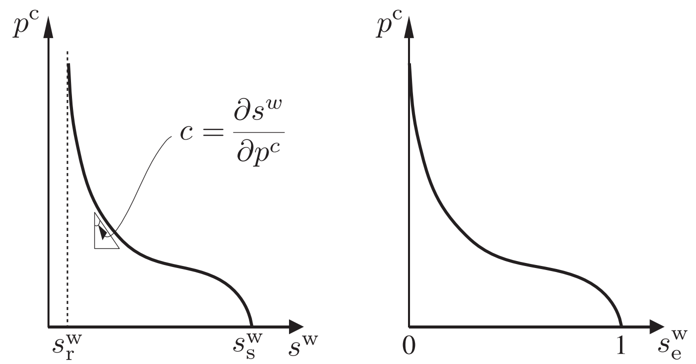

Figure 2. Soil-water characteristics curve and specific moisture capacity.

DOI: 10.1002/nag

$$s_{\mathrm{e}}^{\mathrm{w}} = \frac{s^{\mathrm{w}} - s_{\mathrm{r}}^{\mathrm{w}}}{s_{\mathrm{s}}^{\mathrm{w}} - s_{\mathrm{r}}^{\mathrm{w}}}, \tag{29}$$

where $s_{\mathrm{r}}^{\mathrm{w}}$ is the residual (minimum) degree of water saturation, $s_{\mathrm{s}}^{\mathrm{w}} (= 1 - s_{\mathrm{r}}^{\mathrm{a}})$ is the maximum degree of water saturation, and $s_{\mathrm{r}}^{\mathrm{a}}$ is the residual degree of air saturation. It is noted that VG model is valid only for positive suction $p^{\mathrm{c}} \geqslant 0$. For $p^{\mathrm{c}} < 0$, the effective degree of water saturation $s_{\mathrm{e}}^{\mathrm{w}}$ and the specific moisture capacity c are set to be 1.0 and 0.0, respectively. Hence, the specific moisture capacity c of the VG model is not continuous around $p^{\mathrm{c}} = 0$. The permeability coefficients of water and air with VG model are assumed to be dependent on the effective water saturation as

$$k^{\mathrm{ws}} = k_{\mathrm{s}}^{\mathrm{ws}} \left\{ s_{\mathrm{e}}^{\mathrm{w}} \right\}^{\xi_{\mathrm{vg}}} \left[1 - \left\{ 1 - \left(s_{\mathrm{e}}^{\mathrm{w}} \right)^{\frac{1}{m_{\mathrm{vg}}}} \right\}^{m_{\mathrm{vg}}} \right]^{2} = k_{\mathrm{s}}^{\mathrm{ws}} k_{\mathrm{r}}^{\mathrm{ws}}, \tag{30}$$

$$k^{\mathrm{as}} = k_{\mathrm{s}}^{\mathrm{as}} \left(1 - s_{\mathrm{e}}^{\mathrm{w}} \right)^{\eta_{\mathrm{vg}}} \left\{ 1 - \left(s_{\mathrm{e}}^{\mathrm{w}} \right)^{\frac{1}{m_{\mathrm{vg}}}} \right\}^{2 m_{\mathrm{vg}}} = k_{\mathrm{s}}^{\mathrm{as}} k_{\mathrm{r}}^{\mathrm{as}}, \tag{31}$$

where $k_{\mathrm{s}}^{\mathrm{ws}}$ and $k_{\mathrm{s}}^{\mathrm{as}}$ are the maximum coefficients of water and air permeability, respectively, ξ_{vg} and η_{vg} are the material parameters of VG model, and $k_{\mathrm{r}}^{\mathrm{ws}}$ and $k_{\mathrm{r}}^{\mathrm{as}}$ are the relative permeability coefficients of water and air, respectively.

In the LG model,

$$s_{\mathrm{e}}^{\mathrm{w}} = \left\{ 1 + \exp\left(a_{\mathrm{lg}}\, p^{\mathrm{c}} + b_{\mathrm{lg}} \right) \right\}^{-c_{\mathrm{lg}}}, \tag{32}$$

where a_{lg}, b_{lg}, and c_{lg} are the material parameters of LG model. The LG model is continuous at $p^{\mathrm{c}} = 0$; therefore, the convergence in the iterative numerical scheme can be achieved easier than VG model. In LG model, the permeability coefficients of water and air are assumed to be power functions of the effective water saturation as

$$k^{\mathrm{ws}} = k_{\mathrm{s}}^{\mathrm{ws}} \left(s_{\mathrm{e}}^{\mathrm{w}} \right)^{\xi_{\mathrm{lg}}}, \tag{33}$$

$$k^{\mathrm{as}} = k_{\mathrm{s}}^{\mathrm{as}} \left(1 - s_{\mathrm{e}}^{\mathrm{w}} \right)^{\eta_{\mathrm{lg}}}, \tag{34}$$

where ξ_{lg} and η_{lg} are the material parameters of LG model. The material parameters of VG and LG models can be calibrated in order to fit the model curve to the experimental curve obtained with conventional water retention tests. Typical values of VG model parameters are given in [55].

In the nearly saturated condition, the relative permeability coefficient of air $k_{\mathrm{r}}^{\mathrm{as}}$ is close to zero, whereas in the nearly dry range, it is the relative permeability coefficients of water $k_{\mathrm{r}}^{\mathrm{ws}}$ that is close to zero. In these extreme cases, the infinitesimal relative permeability coefficients of fluids could cause numerical instability as will be shown later. If zero relative permeability coefficients of fluid are used in the continuity equations, the momentum balance equations of fluids cannot be taken into account. To overcome this problem, the lower limits of relative permeability coefficients of fluids are introduced. The lower limits of the relative permeability coefficients of fluids are assumed to be 1.0×10^{-3} for the numerical examples presented in this study.

Finally, the Cauchy effective stress of solid skeleton is assumed as an additive decomposition of the form [8]

$$\boldsymbol{\sigma}' = \boldsymbol{\sigma}_{\mathrm{inv}}' + \boldsymbol{\sigma}_{\mathrm{vis}}', \tag{35}$$

DOI: 10.1002/nag

where $\boldsymbol{\sigma}'_{\text{inv}}$ and $\boldsymbol{\sigma}'_{\text{vis}}$ are the inviscid and viscous parts of $\boldsymbol{\sigma}'$, respectively. The inviscid part of the Cauchy effective stress can be obtained by the hyperelastic constitutive equation (neo-Hookean model [56]) as

$$\boldsymbol{\sigma}'_{\text{inv}} = \frac{\mu}{J^{\text{s}}}(\boldsymbol{b}^{\text{s}} - \boldsymbol{I}) + \frac{\lambda}{J^{\text{s}}}(\ln J^{\text{s}})\boldsymbol{I}, \tag{36}$$

where λ and μ are the Lamé constants of neo-Hookean model. The Jacobian J^{s} is defined as $\det(\boldsymbol{F}^{\text{s}})$ with the deformation gradient $\boldsymbol{F}^{\text{s}}$ of solid skeleton. The left Cauchy-Green tensor $\boldsymbol{b}^{\text{s}}$ of solid skeleton is defined as $\boldsymbol{F}^{\text{s}}(\boldsymbol{F}^{\text{s}})^{\text{T}}$. The viscous part of the Cauchy effective stress for the solid skeleton can be obtained by Kelvin constitutive equation [57] as

$$\boldsymbol{\sigma}'_{\text{vis}} = \alpha_{\text{vis}}\ \boldsymbol{c} : \boldsymbol{d}^{\text{s}}, \tag{37}$$

where α_{vis} is the material parameter reflecting the viscous damping characteristics of the solid skeleton, and $\boldsymbol{d}^{\text{s}}$ is the deformation rate tensor of solid skeleton. The fourth-order spatial elasticity tensor $\boldsymbol{c}$ in the current configuration can be obtained as

$$\boldsymbol{c} = \frac{\lambda}{J^{\text{s}}}\boldsymbol{I}\otimes\boldsymbol{I} + \frac{2}{J^{\text{s}}}(\mu - \lambda \ln J^{\text{s}})\mathcal{I}, \tag{38}$$

where $\mathcal{I}$ is the fourth-order identity tensor.

We use the inviscid hyperelastic constitutive equation for solid skeleton in quasi-static examples and add the viscous part in dynamic examples. The choice of this relatively simple material model allows us to focus more on the formulation and performance of the finite deformation model in the quasi-static and dynamic responses of unsaturated porous structures. Multiplicative plasticity models are based on the framework of hyperelasticity [58], so they can easily be cast within the proposed finite deformation framework.

2.6. Governing equations (full formulation)

Adding the momentum balance equations (12) of three phases with (5) and (13), the momentum balance equation of overall mixture is obtained as

$$\begin{aligned}&\rho\boldsymbol{a}^{\text{s}} + \rho^{\text{w}}\left[\frac{D^{\text{s}}\boldsymbol{v}^{\text{ws}}}{Dt} + \{\text{grad}\,(\boldsymbol{v}^{s} + \boldsymbol{v}^{\text{ws}})\}\boldsymbol{v}^{\text{ws}}\right] + \rho^{\text{a}}\left[\frac{D^{\text{s}}\boldsymbol{v}^{\text{as}}}{Dt} + \{\text{grad}\,(\boldsymbol{v}^{s} + \boldsymbol{v}^{\text{as}})\}\boldsymbol{v}^{\text{as}}\right]\\&= \text{div}\left(\boldsymbol{\sigma}' - \bar{p}\boldsymbol{I}\right) + \rho\boldsymbol{b},\end{aligned} \tag{39}$$

where the body force is assumed to be $\boldsymbol{b}^{\alpha} = \boldsymbol{b}$ for all α phases. Substituting (3), (9), (17), (21), and (23) into the momentum balance of pore water (12), the momentum balance equation of pore water is obtained as

$$\begin{aligned}&ns^{\text{w}}\rho^{\text{wR}}\left[\boldsymbol{a}^{\text{s}} + \frac{D^{\text{s}}\boldsymbol{v}^{\text{ws}}}{Dt} + \{\text{grad}\,(\boldsymbol{v}^{s} + \boldsymbol{v}^{\text{ws}})\}\boldsymbol{v}^{\text{ws}}\right]\\&= -ns^{\text{w}}\ \text{grad}\ p^{\text{w}} + ns^{\text{w}}\rho^{\text{wR}}\boldsymbol{b} - \frac{ns^{\text{w}}\rho^{\text{wR}}g}{k^{\text{ws}}}ns^{\text{w}}\boldsymbol{v}^{\text{ws}}.\end{aligned} \tag{40}$$

Similarly, substituting (4), (10), (18), (22), and (24) into the momentum balance of pore air (12), the momentum balance equation of pore air is obtained as

$$\begin{aligned}&ns^{\text{a}}\rho^{\text{aR}}\left[\boldsymbol{a}^{\text{s}} + \frac{D^{\text{s}}\boldsymbol{v}^{\text{as}}}{Dt} + \{\text{grad}\,(\boldsymbol{v}^{s} + \boldsymbol{v}^{\text{as}})\}\boldsymbol{v}^{\text{as}}\right]\\&= -ns^{\text{a}}\ \text{grad}\ p^{\text{a}} + ns^{\text{a}}\rho^{\text{aR}}\boldsymbol{b} - \frac{ns^{\text{a}}\rho^{\text{aR}}g}{k^{\text{as}}}ns^{\text{a}}\boldsymbol{v}^{\text{as}}.\end{aligned} \tag{41}$$

DOI: 10.1002/nag

Substituting (2) into the mass balance equation of solid skeleton (11),

$$\rho^{\mathrm{sR}} \frac{D^{\mathrm{s}}(1-n)}{Dt} + (1-n)\frac{D^{\mathrm{s}}\rho^{\mathrm{sR}}}{Dt} + (1-n)\rho^{\mathrm{sR}} \operatorname{div} \boldsymbol{v}^{\mathrm{s}} = 0. \tag{42}$$

Similarly, substituting (3) into the mass balance equation of pore water (11),

$$s^{\mathrm{w}}\rho^{\mathrm{wR}}\frac{D^{\mathrm{s}}n}{Dt} + n\rho^{\mathrm{wR}}\frac{D^{\mathrm{s}}s^{\mathrm{w}}}{Dt} + ns^{\mathrm{w}}\frac{D^{\mathrm{s}}\rho^{\mathrm{wR}}}{Dt} + ns^{\mathrm{w}}\rho^{\mathrm{wR}} \operatorname{div} \boldsymbol{v}^{\mathrm{s}} + \operatorname{div}\left(ns^{\mathrm{w}}\rho^{\mathrm{wR}}\boldsymbol{v}^{\mathrm{ws}}\right) = 0. \tag{43}$$

By (42) $\times s^{\mathrm{w}}\rho^{\mathrm{wR}}/\rho^{\mathrm{sR}}$ + (43), the material time derivative of n can be vanished as

$$\frac{(1-n)s^{\mathrm{w}}\rho^{\mathrm{wR}}}{\rho^{\mathrm{sR}}}\frac{D^{\mathrm{s}}\rho^{\mathrm{sR}}}{Dt} + ns^{\mathrm{w}}\frac{D^{\mathrm{s}}\rho^{\mathrm{wR}}}{Dt} + n\rho^{\mathrm{wR}}\frac{D^{\mathrm{s}}s^{\mathrm{w}}}{Dt} + s^{\mathrm{w}}\rho^{\mathrm{wR}} \operatorname{div} \boldsymbol{v}^{\mathrm{s}} + \operatorname{div}\left(ns^{\mathrm{w}}\rho^{\mathrm{wR}}\boldsymbol{v}^{\mathrm{ws}}\right) = 0. \tag{44}$$

Moreover, with (25), (27), and Assumption 2, the continuity equation for pore water with respect to the current configuration of solid skeleton can be obtained as

$$\left(\frac{ns^{\mathrm{w}}\rho^{\mathrm{wR}}}{K^{\mathrm{w}}} - n\rho^{\mathrm{wR}}c\right)\frac{D^{\mathrm{s}}p^{\mathrm{w}}}{Dt} + n\rho^{\mathrm{wR}}c\frac{D^{\mathrm{s}}p^{\mathrm{a}}}{Dt} + s^{\mathrm{w}}\rho^{\mathrm{wR}} \operatorname{div} \boldsymbol{v}^{\mathrm{s}} + \operatorname{div}\left(ns^{\mathrm{w}}\rho^{\mathrm{wR}}\boldsymbol{v}^{\mathrm{ws}}\right) = 0. \tag{45}$$

Similarly, using the mass balance equations for the solid skeleton and pore air with (26), (27), and Assumption 2, the continuity equation of pore air with respect to the current configuration of solid skeleton can be obtained as

$$\left\{\frac{n(1-s^{\mathrm{w}})}{\Theta\bar{R}} - n\rho^{\mathrm{aR}}c\right\}\frac{D^{\mathrm{s}}p^{\mathrm{a}}}{Dt} + n\rho^{\mathrm{aR}}c\frac{D^{\mathrm{s}}p^{\mathrm{w}}}{Dt} + (1-s^{\mathrm{w}})\rho^{\mathrm{aR}} \operatorname{div} \boldsymbol{v}^{\mathrm{s}} + \operatorname{div}\left(ns^{\mathrm{a}}\rho^{\mathrm{aR}}\boldsymbol{v}^{\mathrm{as}}\right) = 0. \tag{46}$$

Equations (39)–(41), (45), and (46) are the governing equations of the full formulations with the primary variables of $\boldsymbol{u}^{\mathrm{s}}$, $\boldsymbol{u}^{\mathrm{ws}}$, $\boldsymbol{u}^{\mathrm{as}}$, p^{w}, and p^{a}.

2.7. Governing equations (simplified formulation)

The additional following assumptions are used for simplicity, as mentioned above: (i) the material time derivatives of relative velocity of the pore fluids to the solid skeleton are ignored as compared to the acceleration of the solid skeleton; (ii) the advection terms of the pore fluids to the solid skeleton are ignored as compared to the acceleration of the solid skeleton. These assumptions are acceptable in the low-frequency range, such as that encountered in geotechnical earthquake engineering applications [13, 68].

Neglecting the primary variables, $\boldsymbol{u}^{\mathrm{ws}}$ and $\boldsymbol{u}^{\mathrm{as}}$, in the above full formulations, the simplified governing equations with the primary variables of solid skeleton displacement $\boldsymbol{u}^{s}$, pore water pressure p^{w}, and pore air pressure p^{a} are derived in this section. The simplified governing equations consist of the momentum balance equations for the overall three-phase material and the mass and momentum balance equations of the pore water and air.

Using the above additional assumptions, together with the momentum balance equation (39) for the overall mixture, the momentum balance equation for total mixture is obtained as

$$\rho\boldsymbol{a}^{\mathrm{s}} = \operatorname{div}\left(\boldsymbol{\sigma}' - \bar{p}\boldsymbol{I}\right) + \rho\boldsymbol{b}, \tag{47}$$

where the second and third terms in the left-hand side of (39) are neglected. In the momentum balance equations for the pore water and air (40) and (41), the generalized Darcy's laws are obtained with the above additional assumptions as

DOI: 10.1002/nag

$$ns^{\mathrm{w}}\boldsymbol{v}^{\mathrm{ws}} = \frac{k^{\mathrm{ws}}}{\rho^{\mathrm{wR}}g}\left\{-\operatorname{grad} p^{\mathrm{w}} + \rho^{\mathrm{wR}}(\boldsymbol{b}^{\mathrm{w}} - \boldsymbol{a}^{\mathrm{s}})\right\}, \tag{48}$$

$$ns^{\mathrm{a}}\boldsymbol{v}^{\mathrm{as}} = \frac{k^{\mathrm{as}}}{\rho^{\mathrm{aR}}g}\left\{-\operatorname{grad} p^{\mathrm{a}} + \rho^{\mathrm{aR}}(\boldsymbol{b}^{\mathrm{a}} - \boldsymbol{a}^{\mathrm{s}})\right\}. \tag{49}$$

Substituting (48) into (45), the mass and momentum balance equation of pore water with respect to the current configuration of solid skeleton is obtained as

$$\begin{aligned}&\left(\frac{ns^{\mathrm{w}}\rho^{\mathrm{wR}}}{K^{\mathrm{w}}} - n\rho^{\mathrm{wR}}c\right)\frac{D^{\mathrm{s}}p^{\mathrm{w}}}{Dt} + n\rho^{\mathrm{wR}}c\frac{D^{\mathrm{s}}p^{\mathrm{a}}}{Dt} + s^{\mathrm{w}}\rho^{\mathrm{wR}}\operatorname{div}\boldsymbol{v}^{\mathrm{s}}\\ &+\operatorname{div}\left\{\frac{k^{\mathrm{ws}}}{g}\left(-\operatorname{grad} p^{\mathrm{w}} + \rho^{\mathrm{wR}}\boldsymbol{b} - \rho^{\mathrm{wR}}\boldsymbol{a}^{\mathrm{s}}\right)\right\} = 0.\end{aligned} \tag{50}$$

Similarly, substituting (49) into (46), the mass and momentum balance equation of pore air with respect to the current configuration of solid skeleton is obtained as

$$\begin{aligned}&\left\{\frac{n(1-s^{\mathrm{w}})}{\Theta\bar{R}} - n\rho^{\mathrm{aR}}c\right\}\frac{D^{\mathrm{s}}p^{\mathrm{a}}}{Dt} + n\rho^{\mathrm{aR}}c\frac{D^{\mathrm{s}}p^{\mathrm{w}}}{Dt} + (1-s^{\mathrm{w}})\rho^{\mathrm{aR}}\operatorname{div}\boldsymbol{v}^{\mathrm{s}}\\ &+\operatorname{div}\left\{\frac{k^{\mathrm{as}}}{g}\left(-\operatorname{grad} p^{\mathrm{a}} + \rho^{\mathrm{aR}}\boldsymbol{b} - \rho^{\mathrm{aR}}\boldsymbol{a}^{\mathrm{s}}\right)\right\} = 0.\end{aligned} \tag{51}$$

The fourth terms in the left-hand sides of equations (50) and (51) contain the momentum balance equations of fluids. Therefore, the momentum balance equations of fluids cannot be taken into account if zero permeability coefficients of fluid are used. To overcome this problem, the lower limits of relative permeability coefficients of fluids are introduced as mentioned before. Equations (47), (50), and (51) are the simplified governing equations of $\boldsymbol{u}^{\mathrm{s}} - p^{\mathrm{w}} - p^{\mathrm{a}}$ formulation. The simplified governing equations are solved with the finite element method. A time integration scheme is presented in the following section.

3. FINITE ELEMENT FORMULATION

The finite element method is used for the spatial discretization, and Newmark integration scheme is used for the time discretization. The weak forms obtained by conventional Galerkin method in the current configuration are nonlinear equations with respect to the primary variables ($\boldsymbol{u}^{\mathrm{s}}$, p^{w}, and p^{a}) and the current configuration $\boldsymbol{x}$. Therefore, the weak forms are iteratively solved with Newton-Raphson method. In this iterative scheme, the weak forms are linearized with respect to the primary variables.

3.1. Weak forms

The governing equations of the boundary-value problem for a simple body B^{s} with boundary ∂B^{s} in the current configuration of the solid skeleton consist of the strong forms ((47), (50), and (51)) and the following boundary conditions.

$$\boldsymbol{u}^{\mathrm{s}} = \bar{\boldsymbol{u}}^{\mathrm{s}} \quad \text{on } \partial B^{\mathrm{s}}_{\mathrm{u}}, \tag{52}$$

DOI: 10.1002/nag

$$\boldsymbol{\sigma n} = (\boldsymbol{\sigma}' - \overline{p}\boldsymbol{I})\boldsymbol{n} = \overline{\boldsymbol{t}} \quad \text{on } \partial B^{\mathrm{s}}_{\mathrm{t}}, \tag{53}$$

$$p^{\mathrm{w}} = \overline{p}^{\,w} \quad \text{on } \partial B^{\mathrm{s}}_{\mathrm{wp}}, \tag{54}$$

$$ns^{\mathrm{w}}\rho^{\mathrm{wR}}\boldsymbol{v}^{\mathrm{ws}}\cdot\boldsymbol{n} = \boldsymbol{q}^{\mathrm{w}}\cdot\boldsymbol{n} = \overline{q}^{\,w} \quad \text{on } \partial B^{\mathrm{s}}_{\mathrm{wq}}, \tag{55}$$

$$p^{\mathrm{a}} = \overline{p}^{\,\mathrm{a}} \quad \text{on } \partial B^{\mathrm{s}}_{\mathrm{ap}}, \tag{56}$$

$$ns^{\mathrm{a}}\rho^{\mathrm{aR}}\boldsymbol{v}^{\mathrm{as}}\cdot\boldsymbol{n} = \boldsymbol{q}^{\mathrm{a}}\cdot\boldsymbol{n} = \overline{q}^{\,\mathrm{a}} \quad \text{on } \partial B^{\mathrm{s}}_{\mathrm{aq}}, \tag{57}$$

where $\overline{\boldsymbol{u}}^{\mathrm{s}}$ is the prescribed displacement vector of solid skeleton at $\partial B^{\mathrm{s}}_{\mathrm{u}}$, $\overline{p}^{\,\mathrm{w}}$ and $\overline{p}^{\mathrm{a}}$ are the prescribed pore water and air pressures at $\partial B^{\mathrm{s}}_{\mathrm{wp}}$ and $\partial B^{\mathrm{s}}_{\mathrm{ap}}$, respectively. $\overline{\boldsymbol{t}}$ is the prescribed traction vector at $\partial B^{\mathrm{s}}_{\mathrm{t}}$, and $\overline{q}^{\,\mathrm{w}}$ and $\overline{q}^{\,\mathrm{a}}$ are the prescribed mass flux on a unit area with unit normal vector $\boldsymbol{n}$ at $\partial B^{\mathrm{s}}_{\mathrm{wq}}$ and $\partial B^{\mathrm{s}}_{\mathrm{aq}}$, respectively. The decomposed boundaries hold

$$\begin{aligned} \partial B^{\mathrm{s}} = \partial B^{\mathrm{s}}_{\mathrm{u}} \cup \partial B^{\mathrm{s}}_{\mathrm{t}} = \partial B^{\mathrm{s}}_{\mathrm{wp}} \cup \partial B^{\mathrm{s}}_{\mathrm{wq}} = \partial B^{\mathrm{s}}_{\mathrm{ap}} \cup \partial B^{\mathrm{s}}_{\mathrm{aq}} \\ \partial B^{\mathrm{s}}_{\mathrm{u}} \cap \partial B^{\mathrm{s}}_{\mathrm{t}} = \partial B^{\mathrm{s}}_{\mathrm{wp}} \cap \partial B^{\mathrm{s}}_{\mathrm{wq}} = \partial B^{\mathrm{s}}_{\mathrm{ap}} \cap \partial B^{\mathrm{s}}_{\mathrm{aq}} = 0. \end{aligned} \tag{58}$$

Considering the arbitrary test function $\delta\boldsymbol{v}^{\mathrm{s}}$ that satisfies

$$\delta\boldsymbol{v}^{\mathrm{s}} = \boldsymbol{0} \quad \text{on } \partial B^{\mathrm{s}}_{\mathrm{u}}, \tag{59}$$

the weak form of the momentum balance equation (47) and the natural boundary conditions (53) is obtained in the current configuration as

$$\delta w^{\mathrm{s}} = \int_{B^s} \rho\delta\boldsymbol{v}^{\mathrm{s}}\cdot\boldsymbol{a}^{\mathrm{s}}\, dv + \int_{B^s} \delta\boldsymbol{d}^{\mathrm{s}} : \boldsymbol{\sigma}' dv - \int_{B^s} \overline{p}\; div\; \delta\boldsymbol{v}^{\mathrm{s}} dv - \int_{B^s} \rho\delta\boldsymbol{v}^{\mathrm{s}}\cdot\boldsymbol{b}dv - \int_{\partial B^s_{\mathrm{t}}} \delta\boldsymbol{v}^{\mathrm{s}}\cdot\overline{\boldsymbol{t}}da = 0. \tag{60}$$

Considering the arbitrary test function δp^{w} that satisfies

$$\delta p^{\mathrm{w}} = 0 \quad \text{on } \partial B^{\mathrm{s}}_{\mathrm{wp}}, \tag{61}$$

the weak form of the mass and momentum balance equation of pore water (50) and the natural boundary conditions (55) is obtained in the current configuration as

$$\begin{aligned} \delta w^{\mathrm{w}} = & \int_{B^{\mathrm{s}}} \delta p^{\mathrm{w}} \left(\frac{ns^{\mathrm{w}}\rho^{\mathrm{wR}}}{K^{\mathrm{w}}} - n\rho^{\mathrm{wR}}c \right) \frac{D^{\mathrm{s}}p^{\mathrm{w}}}{Dt} dv + \int_{B^{\mathrm{s}}} \delta p^{\mathrm{w}} n\rho^{\mathrm{wR}} c \frac{D^{\mathrm{s}}p^{\mathrm{a}}}{Dt} dv \\ & + \int_{B^{\mathrm{s}}} \delta p^{\mathrm{w}} s^{\mathrm{w}}\rho^{\mathrm{wR}}\,\mathrm{div}\,\boldsymbol{v}^{\mathrm{s}} dv - \int_{B^{\mathrm{s}}} \mathrm{grad}\,\delta p^{\mathrm{w}} \cdot \left\{ \frac{k^{\mathrm{ws}}}{g} \left(-\,\mathrm{grad}\,p^{\mathrm{w}} + \rho^{\mathrm{wR}}\boldsymbol{b} - \rho^{\mathrm{wR}}\boldsymbol{a}^{\mathrm{s}} \right) \right\} dv \\ & + \int_{\partial B^{\mathrm{s}}_{\mathrm{wq}}} \delta p^{\mathrm{w}}\overline{q}^{\mathrm{w}} da = 0. \end{aligned} \tag{62}$$

Similarly, considering the arbitrary test function δp^{a} that satisfies

$$\delta p^{\mathrm{a}} = 0 \quad \text{on } \partial B^{\mathrm{s}}_{\mathrm{ap}}, \tag{63}$$

the weak form of the mass and momentum balance equation of pore air (51) and the natural boundary conditions (57) is obtained in the current configuration as

$$
\begin{aligned}
\delta w^{\mathrm{a}} = & \int_{B^{\mathrm{s}}} \delta p^{\mathrm{a}} \left(\frac{n(1-s^{\mathrm{w}})}{\Theta \bar{R}} - n\rho^{\mathrm{aR}} c \right) \frac{D^{\mathrm{s}} p^{\mathrm{a}}}{Dt} dv + \int_{B^{\mathrm{s}}} \delta p^{\mathrm{a}} n \rho^{\mathrm{aR}} c \frac{D^{\mathrm{s}} p^{\mathrm{w}}}{Dt} dv \\
& + \int_{B^{\mathrm{s}}} \delta p^{\mathrm{a}} (1-s^{\mathrm{w}}) \rho^{\mathrm{aR}} \ \operatorname{div} \boldsymbol{v}^{\mathrm{s}} dv - \int_{B^{\mathrm{s}}} \ \operatorname{grad} \delta p^{\mathrm{a}} \cdot \left\{ \frac{k^{\mathrm{as}}}{g} \left(-\operatorname{grad} p^{\mathrm{a}} + \rho^{\mathrm{aR}} \boldsymbol{b} - \rho^{\mathrm{aR}} \boldsymbol{a}^{\mathrm{s}} \right) \right\} dv \\
& + \int_{\partial B^{\mathrm{s}}_{\mathrm{aq}}} \delta p^{\mathrm{a}} \bar{q}^{\mathrm{a}} da = 0.
\end{aligned} \tag{64}
$$

3.2. Time integration

In dynamic analyses, the Newmark time integration scheme is used for the displacement of the solid skeleton:

$$\boldsymbol{u}^{\mathrm{s}} = \boldsymbol{u}^{\mathrm{s}}_t + \Delta t \boldsymbol{v}^{\mathrm{s}}_t + \frac{1}{2} \Delta t^2 (1-2\beta) \boldsymbol{a}^{\mathrm{s}}_t + \beta \Delta t^2 \boldsymbol{a}^{\mathrm{s}}, \tag{65}$$

$$\boldsymbol{v}^{\mathrm{s}} = \boldsymbol{v}^{\mathrm{s}}_t + (1-\gamma) \Delta t \, \boldsymbol{a}^{\mathrm{s}}_t + \gamma \Delta t \, \boldsymbol{a}^{\mathrm{s}}, \tag{66}$$

where the subscript t denotes the previous time. The variables with the subscript t are known at the current time and are constant during Newton-Raphson iteration; Δt is the time increment, and β and γ are the numerical parameters. Similarly, the evolutions of pore water and air pressures are expressed as

$$p^{\mathrm{w}} = p^{\mathrm{w}}_t + \Delta t \ \dot{p}^{\mathrm{w}}_t + \frac{1}{2} \Delta t^2 (1-2\beta) \ddot{p}^{\mathrm{w}}_t + \beta \Delta t^2 \ddot{p}^{\mathrm{w}}, \tag{67}$$

$$\dot{p}^{\mathrm{w}} = \ \dot{p}^{\mathrm{w}}_t + (1-\gamma) \Delta t \ddot{p}^{\mathrm{w}}_t + \gamma \Delta t \ddot{p}^{\mathrm{w}}, \tag{68}$$

$$p^{\mathrm{a}} = p^{\mathrm{a}}_t + \Delta t \ \dot{p}^{\mathrm{a}}_t + \frac{1}{2} \Delta t^2 (1-2\beta) \ddot{p}^{\mathrm{a}}_t + \beta \Delta t^2 \ddot{p}^{\mathrm{a}}, \tag{69}$$

$$\dot{p}^{\mathrm{a}} = \ \dot{p}^{\mathrm{a}}_t + (1-\gamma) \Delta t \ddot{p}^{\mathrm{a}}_t + \gamma \Delta t \ddot{p}^{\mathrm{a}}, \tag{70}$$

where $\dot{\square}$ $(= D^s \square / Dt)$ denotes the material time derivative of $\square$ with respect to the solid skeleton.

In quasi-static analyses, only the velocity components are considered, and the equations take the following forms:

$$\boldsymbol{u}^{\mathrm{s}} = \boldsymbol{u}^{\mathrm{s}}_t + (1-\gamma) \Delta t \boldsymbol{v}^{\mathrm{s}}_t + \gamma \Delta t \boldsymbol{v}^{\mathrm{s}}, \tag{71}$$

$$p^{\mathrm{w}} = p^{\mathrm{w}}_t + (1-\gamma) \Delta t \ \dot{p}^{\mathrm{w}}_t + \gamma \Delta t \ \dot{p}^{\mathrm{w}}, \tag{72}$$

$$p^{\mathrm{a}} = p^{\mathrm{a}}_t + (1-\gamma) \Delta t \ \dot{p}^{\mathrm{a}}_t + \gamma \Delta t \ \dot{p}^{\mathrm{a}}. \tag{73}$$

3.3. Newton-Raphson method

The weak forms ((60), (62), and (64)) in the current configuration are nonlinear equations with respect to the primary variables ($\boldsymbol{u}^{\mathrm{s}}$, p^{w}, and p^{a}) at the current configuration $\boldsymbol{x}$.

$$
\begin{aligned}
\delta w^{\mathrm{s}} \left(\boldsymbol{a}^{\mathrm{s}}, \ddot{p}^{\mathrm{w}}, \ddot{p}^{\mathrm{a}} \right) = 0, \\
\delta w^{\mathrm{w}} \left(\boldsymbol{a}^{\mathrm{s}}, \ddot{p}^{\mathrm{w}}, \ddot{p}^{\mathrm{a}} \right) = 0, \\
\delta w^{\mathrm{a}} \left(\boldsymbol{a}^{\mathrm{s}}, \ddot{p}^{\mathrm{w}}, \ddot{p}^{\mathrm{a}} \right) = 0.
\end{aligned} \tag{74}
$$

DOI: 10.1002/nag

Taking the directional derivative [4, 5, 56, 59] of the left-hand side terms with respect to the second-order material time derivative of the primary variables and the current configuration, the weak forms are linearized and iteratively solved with Newton-Raphson method. The linearized formulations of these equations are obtained as

$$\begin{aligned} D\delta w^{\mathrm{s}}[\Delta \boldsymbol{a}^{\mathrm{s}}] + D\delta w^{\mathrm{s}}\left[\Delta \ddot{p}^{\mathrm{w}}\right] + D\delta w^{\mathrm{s}}\left[\Delta \ddot{p}^{\mathrm{a}}\right] &= -\delta w^{\mathrm{s}}_{k}, \\ D\delta w^{\mathrm{w}}[\Delta \boldsymbol{a}^{\mathrm{s}}] + D\delta w^{\mathrm{w}}\left[\Delta \ddot{p}^{\mathrm{w}}\right] + D\delta w^{\mathrm{w}}\left[\Delta \ddot{p}^{\mathrm{a}}\right] &= -\delta w^{\mathrm{w}}_{k}, \\ D\delta w^{\mathrm{a}}[\Delta \boldsymbol{a}^{\mathrm{s}}] + D\delta w^{\mathrm{a}}\left[\Delta \ddot{p}^{\mathrm{w}}\right] + D\delta w^{\mathrm{a}}\left[\Delta \ddot{p}^{\mathrm{a}}\right] &= -\delta w^{\mathrm{a}}_{k}, \end{aligned} \tag{75}$$

where $\Delta \boldsymbol{a}^{\mathrm{s}}$, $\Delta \ddot{p}^{\mathrm{w}}$, and $\Delta \ddot{p}^{\mathrm{a}}$ are the variations at the current iterative step $k+1$. The right-hand side terms are the residual of $\delta w^{\mathrm{s}}_{k}$, $\delta w^{\mathrm{w}}_{k}$ and $\delta w^{\mathrm{a}}_{k}$ at the previous iterative step k. D□ [Δ●] denotes the directional derivative of □ with respect to •. It is convenient to linearize the weak forms transformed to the reference configuration by a pull-back operation because the initial volume dV^{s} in the reference configuration is constant during the linearization. The linearized weak forms in the reference configuration then are transformed by a push forward operation to the current configuration. The details of the linearized weak forms are described in Appendix . The solutions at the current iterative step $k+1$ are obtained as

$$\begin{aligned} \boldsymbol{a}^{\mathrm{s}}_{k+1} &= \boldsymbol{a}^{\mathrm{s}}_{k} + \Delta \boldsymbol{a}^{\mathrm{s}}, \\ \ddot{p}^{\mathrm{w}}_{k+1} &= \ddot{p}^{\mathrm{w}}_{k} + \Delta \ddot{p}^{\mathrm{w}}, \\ \ddot{p}^{\mathrm{a}}_{k+1} &= \ddot{p}^{\mathrm{a}}_{k} + \Delta \ddot{p}^{\mathrm{a}}. \end{aligned} \tag{76}$$

The iteration continues until the norms of the residual vectors of $\delta w^{\mathrm{s}}_{k}$, $\delta w^{\mathrm{w}}_{k}$, and $\delta w^{\mathrm{s}}_{a}$ are smaller than a specified error tolerance. The integrated variables, such as displacement and pressure, can be calculated with integration equations from (65) to (70). In quasi-static analyses, the weak forms are linearized with respect to the first-order material time derivative of the primary variables $\varDelta \boldsymbol{v}^{\mathrm{s}}$, $\Delta\, \dot{p}^{\mathrm{w}}$, and $\Delta\, \dot{p}^{\mathrm{a}}$, and the integrated variables can be calculated with equations from (71) to (73).

3.4. Finite element

The finite element formulation in the current configuration is derived by applying the standard Galerkin method in which the test functions are approximated by the same shape functions used to approximate the primary variables. The different shape functions between solid skeleton and pore fluid are used for the approximations of the displacement and pressures to satisfy the discrete LBB conditions [60, 61] for the locally undrained case at infinitesimal deformation. In the following numerical examples under plane strain condition, an isoparametric eight-node mixed finite element (Q8P4) interpolation is used. The displacement of the solid skeleton is interpolated using the eight-node serendipity interpolation function N^{s}_{n}:

$$\boldsymbol{u}^{\mathrm{s}}_{e} = \sum_{n=1}^{8} N^{\mathrm{s}}_{n} \boldsymbol{u}^{\mathrm{s}}_{n}, \tag{77}$$

where $\boldsymbol{u}^{\mathrm{s}}_{e}$ is the approximated displacement of solid skeleton in the element, and $\boldsymbol{u}^{\mathrm{s}}_{n}$ is the displacement at the eight nodes. The pore water and pore air pressures are approximated with bilinear interpolation function N^{f}_{n}:

$$p^{\mathrm{w}}_{e} = \sum_{n=1}^{4} N^{\mathrm{f}}_{n} p^{\mathrm{w}}_{n}, \quad p^{\mathrm{a}}_{e} = \sum_{n=1}^{4} N^{\mathrm{f}}_{n} p^{\mathrm{a}}_{n}, \tag{78}$$

where p^{w}_{e} and p^{a}_{e} are the approximated pore water and pore air pressures, respectively, in the element; and p^{w}_{n} and p^{a}_{n} are the pore water and air pressure, respectively, at the four corner nodes of the mixed element.

4. NUMERICAL EXAMPLES

In this section, we present one-dimensional and two-dimensional (plane strain) examples highlighting the difference between the small and finite deformation analyses of fully and partially saturated elastic porous media. In some examples, the numerical results are validated through comparison with analytical solutions or experimental results. Because the solid matrix is modeled by a neo-Hookean hyperelastic material, which does not capture stiffness degradation, we use either a soft material or a very large load in some examples to magnify the effect of finite deformation.

Two finite element codes are used for this purpose: one is based on the infinitesimal formulation in which the geometric effects are completely ignored, and another is based on the proposed finite deformation theory. Both the infinitesimal and finite deformation codes utilize the Q8P4 mixed finite elements for the spatial interpolation of the solid displacement and fluid pressure, and the Newmark time integration scheme employing the same time-integration parameters. In the infinitesimal regime, the neo-Hookean hyperelastic solid reduces to the conventional Hookean material of linear elasticity, making the comparison between the infinitesimal and finite deformation solutions meaningful.

4.1. *Quasi-static consolidation of saturated poroelastic material*

First, we consider the one-dimensional quasi-static consolidation problem with finite deformation. Although the problem is one-dimensional, we model it as a plane strain problem consisting of a saturated solid matrix column 10 m deep with 100 elements in Figure 3. The upper boundary is perfectly drained and subjected to a step load of intensity 10 kPa. The lateral boundaries are fixed in the horizontal direction and impermeable. The bottom boundary is rigid and impermeable. Table I shows the material parameters for the saturated poroelastic material. As a fully saturated column is assumed, only the water phase is considered as pore fluid. The compressibility of pore water is ignored. The external load is the surface step load only; the gravity force is not considered. A time increment of calculation varies from 0.1 to 80.0 s with the progress of consolidation. The coefficient in Newmark integration method is $\gamma = 1.0$. The error tolerance for the norm of residual vector is 1.0×10^{-8}.

The numerical results are compared to the analytical solutions for one-dimensional consolidation at small deformation presented by Terzaghi [52]. The analytical solutions for one-dimensional consolidation at finite deformation have been obtained in [62–65]; the following solution by Morris [64] is compared here. The distribution of normalized void ratio E with surface drainage and surface step loading is obtained as

$$E = R + \frac{4}{\pi}(1-R) \sum_{n=1,3,5}^{\infty} \left[\frac{1}{n} \sin\left(\frac{n\pi Z}{2}\right) \exp\left(\frac{-n^2\pi^2 T}{4}\right) \right], \tag{79}$$

where $R = E|_{Z=0}$, and the normalized void ratio E, dimensionless vertical material coordinate Z and dimensionless time factor T are defined as

$$E(Z, T) = \frac{e(z, t)}{e(0, 0)}, \tag{80}$$

$$Z = \frac{z}{\ell}, \tag{81}$$

$$T = \frac{g' t}{\ell^2}, \; g' = -\frac{k}{\gamma_w(1+e)} \frac{\partial \sigma'}{\partial e}, \tag{82}$$

where e is the void ratio, z is the material coordinate of the solid skeleton, ℓ is the height of solid layer, and g' is the finite strain coefficient of consolidation. g' is assumed to be constant in the analytical solution. In order to compare the analytical solution with the proposed numerical solutions, the stress strain relationship in $\partial\sigma'/\partial e$ is calculated with the hyperelastic neo-Hookean model by (36). The vertical Cauchy effective stress σ'_{y} in one-dimensional problem is obtained as

$$\sigma'_{\mathrm{y}} = \frac{\mu}{J^{\mathrm{s}}}\left((J^{\mathrm{s}})^2 - 1\right) + \frac{\lambda}{J^{\mathrm{s}}} \ln J^{\mathrm{s}}. \tag{83}$$

DOI: 10.1002/nag

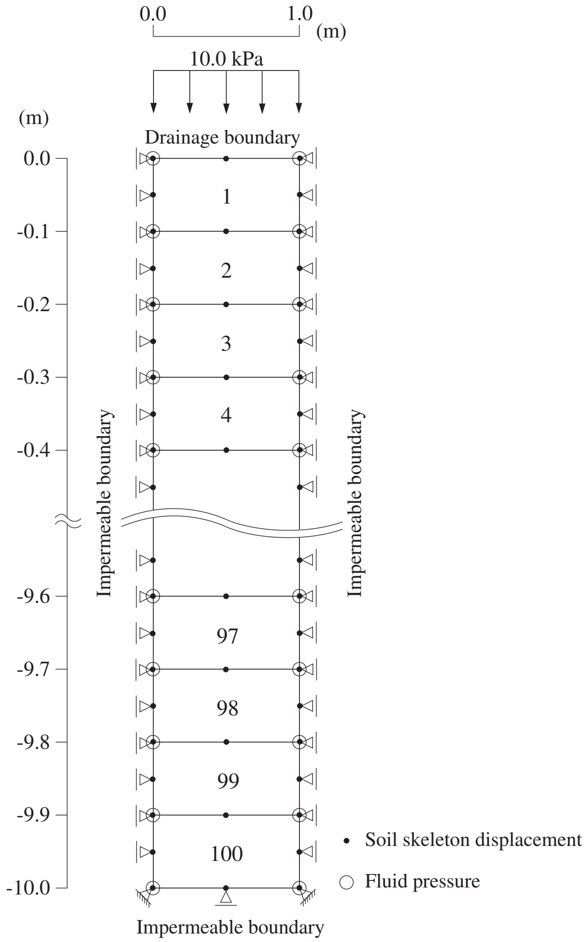

Figure 3. Finite element model in quasi-static consolidation.

Table I. Material parameters in quasi-static consolidation.

Parameter	Symbol	Value
Intrinsic density of solid particle	ρ^{sR} (t/m^3)	1.0
Intrinsic density of fluid	ρ^{wR}_{s0} (t/m^3)	1.0
Initial porosity	n_{s0}	0.5
Coefficient water permeability	k^{ws}_{s0} (m/s)	1.0×10^{-2}
Lamé constant	λ (kN/m^2)	10.0
Lamé constant	$\boldsymbol{\mu}$ (kN/m^2)	15.0
Gravity force	g (m/s^2)	0.0

The subscript “s0” denotes the initial value in the reference configuration of solid skeleton.

The derivative of effective stress with respect to the void ratio is obtained as

$$\frac{\partial \sigma'_{\mathrm{y}}}{\partial e} = \frac{\partial \sigma'_{\mathrm{y}}}{\partial J^{\mathrm{s}}}\frac{\partial J^{\mathrm{s}}}{\partial e} = \left\{\mu\left(1+\frac{1}{(J^{\mathrm{s}})^2}\right)+\frac{\lambda}{(J^{\mathrm{s}})^2}\left(1-\ln J^{\mathrm{s}}\right)\right\}\frac{1}{1+e_0}, \tag{84}$$

where e_0 is the initial void ratio. The Jacobian J^{s} in one-dimensional problem can be expressed as

$$J^{\mathrm{s}} = \frac{1+e}{1+e_0}. \tag{85}$$

DOI: 10.1002/nag

In the numerical simulation, the permeability coefficient of water is dependent on the volumetric change J^s to make the finite strain coefficient of consolidation g' constant.

$$k^{ws}(e) = k_{0s}^{ws} J^s \frac{\left(\partial\sigma_y'/\partial e\right)_{0s}}{\partial\sigma'_y/\partial e} = k_{0s}^{ws} \frac{(2\mu+\lambda)J^s}{\mu\left(1+1/(J^s)^2\right)+(1-\ln J^s)\lambda/(J^s)^2}, \tag{86}$$

where the subscript "0s" pertains to the value in the reference configuration of solid skeleton.

Figure 4 shows the time histories of the vertical displacement at the surface. The top of the figure shows the numerical solution at finite deformation and the bottom shows the solution at small deformation. In both cases, the numerical solutions agree with the analytical solutions. The amplitude of vertical displacement calculated by the small deformation analyses is larger than that calculated by the finite deformation analyses because of geometrical changes. If the permeability coefficient is independent of the volumetric change J^s in the finite deformation analyses, then the vertical displacement approaches the steady-state value sooner for the finite deformation case as compared to the infinitesimal deformation case because the former accounts for the shortening of the drainage distance with vertical compression.

In the finite deformation analyses, the required number of iterations for convergence is six during the early part of pore pressure dissipation and decreases to two as condition approaches the steady state.

4.2. *Quasi-static leaking flow of unsaturated soil*

For the second set of examples, we use the numerical model to reproduce the experimental results on a quasi-static leaking flow in a deformable unsaturated soil. The leaking flow application is well known as a benchmark experiment conducted by Liakopoulos [66]. Liakopoulos measured the leaking flow amount of an initially saturated soil column of fine Del Monte sand under the effect of gravitational forces. In the experiment, the soil column was contained in an impermeable cylindrical vessel open at the bottom and at the top so that one-dimensional flow and deformation would occur. The diameter and height of the soil column were 10 cm and 100 cm, respectively. This test problem has been simulated in [67–69] for numerical method validation purposes.

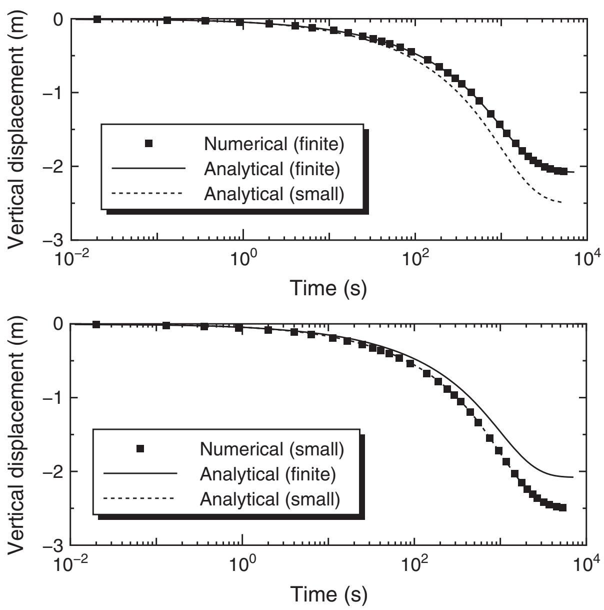

Figure 4. Analytical and numerical solutions in the quasi-static consolidation (top: finite deformation, bottom: small deformation).

DOI: 10.1002/nag

All phases including the pore air are considered in the quasi-static simulations. Figure 5 shows the finite element model used in the simulations. The total height is 1 m, the width is 0.1 m, and the column is divided into 20 eight-node elements. The nodes at the bottom are fixed in vertical and horizontal directions. Other nodes are fixed only in the horizontal direction but are free to move in the vertical direction. Water drainage is allowed only from the bottom, but air drainage is allowed at both the top and bottom surfaces. The material constants, shown in Table II, are the same as those used by Ehlers *et al.* [69]. Figure 6 shows the SWCC and the relationship between the relative permeability of water and air and the effective degree of water saturation by the VG model. Before the leaking analyses, the initial saturated state is obtained with the self-weight analysis under the same boundary condition as the leaking analyses except that the bottom was assumed impermeable. A time increment of calculation varies from 1.0 to 10.0 s. The coefficient in Newmark integration method is $\gamma = 1.0$. The error tolerance on the norm of residual vector is 1.0×10^{-8}.

Two cases are considered as follows: In Case 1, the material parameters shown in Table II are used to reproduce the experimental results. In Case 2, smaller values of the Lamé constants are used to reproduce the large settlement observed during leaking. The intrinsic density of the solid is set to 1.0 to avoid excessively large compression during the initial condition of gravity load application. In Case 2, the influence of deformation of the solid skeleton on the leaking flow in an unsaturated poroelastic material examined further. The difference in the numerical results between the small and finite deformation analyses is examined.

Figure 7 shows the time histories of filter velocity of leaking flow at the bottom. The numerical result reproduces the measured filter velocity. Figure 8 shows the distributions of pore water pressure, pore air pressure, suction, and degree of water saturation in the unsaturated soil column. The leaking at the bottom causes a negative pore water pressure in the saturated soil column. Although the pore air

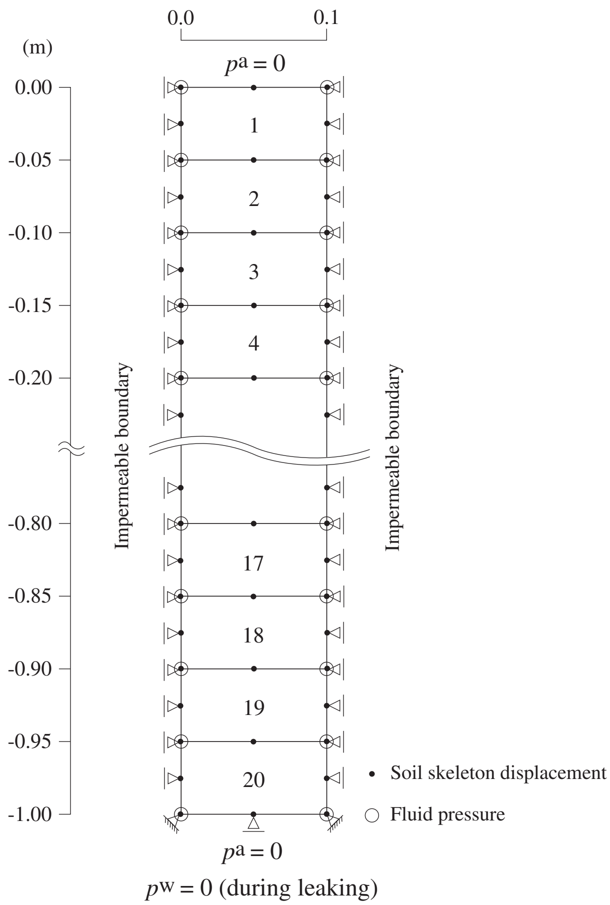

Figure 5. Finite element model in quasi-static leaking flow.

DOI: 10.1002/nag

Table II. Material parameters in quasi-static leaking flow.

Parameter	Symbol	Case 1	Case 2
Intrinsic density of solid particle	ρ^{sR} (t/m^3)	2.72	1.0
Intrinsic density of pore water	ρ_{0s}^{wR} (t/m^3)	1.0	1.0
Intrinsic density of pore air	ρ_{0s}^{aR} (t/m^3)	1.23×10^{-3}	1.23×10^{-3}
Initial porosity	n_{0s}	0.37	0.37
Saturated permeability coefficient for water	k_{0s}^{ws} (m/s)	4.5×10^{-6}	4.5×10^{-6}
Saturated permeability coefficient for air	k_{0s}^{as} (m/s)	3.0×10^{-7}	3.0×10^{-7}
Bulk modulus of water	K^w (kN/m^2)	1.0×10^8	1.0×10^8
Air constant	$1/(\Theta\bar{R})$(s^2/m^2)	1.23×10^{-5}	1.23×10^{-5}
Minimum degree of water saturation	s_r^w	0.02	0.02
Maximum degree of water saturation	s_s^w	1.0	1.0
Parameters in VG model	α_{vg}	0.02	0.02
Parameters in VG model	n_{vg}	1.5	1.5
Parameters in VG model	m_{vg}	1.03	1.03
Parameters in VG model	ξ_{vg}	3.5	3.5
Parameters in VG model	η_{vg}	0.333	0.333
Lamé constant	λ (kN/m^2)	1857.0	15.0
Lamé constant	μ (kN/m^2)	464.0	10.0
Gravity force	g (m/s^2)	−9.8	−9.8

The subscript "0s" denotes the initial value in the reference configuration of solid skeleton.

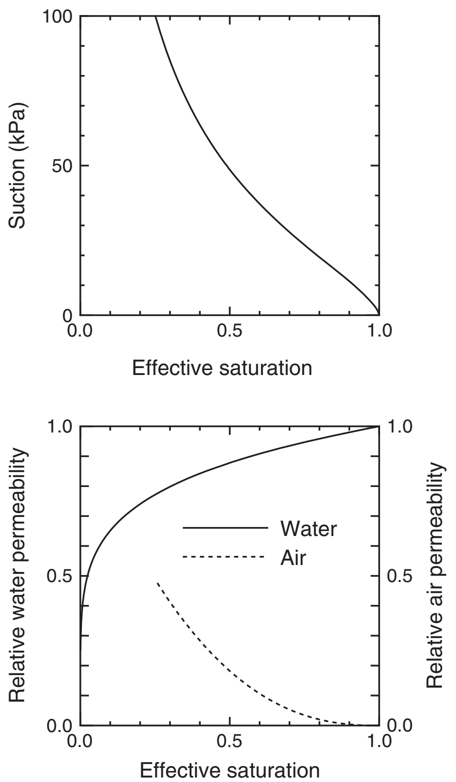

Figure 6. SWCC (top) and relative permeability (bottom) by VG model with the parameters in Table II.

pressure also becomes negative, it vanishes with time because of the air inflow through the specimen's top surface. A positive suction is generated underneath the surface after about 5 min, and it spreads toward the bottom with time progress. The vertical distribution of the suction is not linear with respect to the depth because of the existence of pore air pressure. It is noted that this effect exhibits the major difference between the three-phase and two-phase formulations [67, 69]. Corresponding to the suction behavior, the degree of water saturation decreases from the surface because of the leaking.

DOI: 10.1002/nag

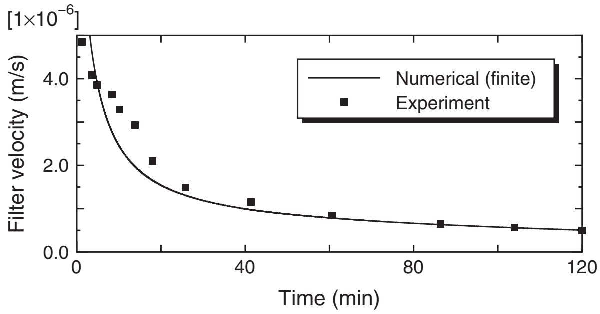

Figure 7. Time histories of leaking from at the bottom in Case 1.

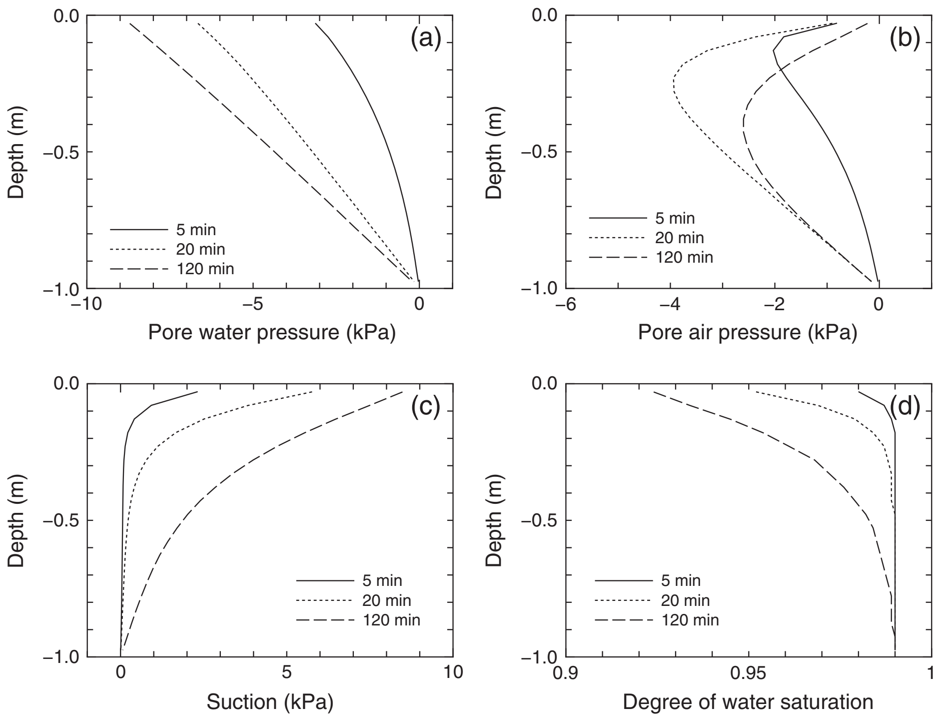

Figure 8. Distributions of (a) pore water and (b) air pressures, (c) suction, and (d) degree of water saturation in Case 1.

In Case 1, the residual settlement is about 0.5 cm much smaller than the height of soil column; therefore, the difference between the small and finite deformation analyses can be ignored. In Case 2, in which smaller stiffness of solid skeleton is used, the difference will appear clearly. Figure 9 shows the time histories of filter velocity of leaking flow at the bottom and vertical displacement at the surface in Case 2. In Case 2, the porosity of the solid skeleton deceases from the bottom because of the drainage of pore water because the soft solid is easy to deform; therefore, the flux velocity at the bottom is much larger than that in Case 1. The compressibility of the solid skeleton significantly affects the leaking flow in the unsaturated soft poroelastic material. The amplitude of vertical displacement by the small deformation analyses is larger than that by the finite deformation analyses because of geometrical changes as well as the consolidation problem in the previous section. The filter velocity of leaking flow at the bottom by the small deformation analyses is larger than that by the finite deformation analyses corresponding to the deformation behavior.

In the finite deformation analyses of Case 1, the converged iteration number at each calculation step is four times at the start and decreases to two times at the end of leaking. Meanwhile, in the finite

DOI: 10.1002/nag

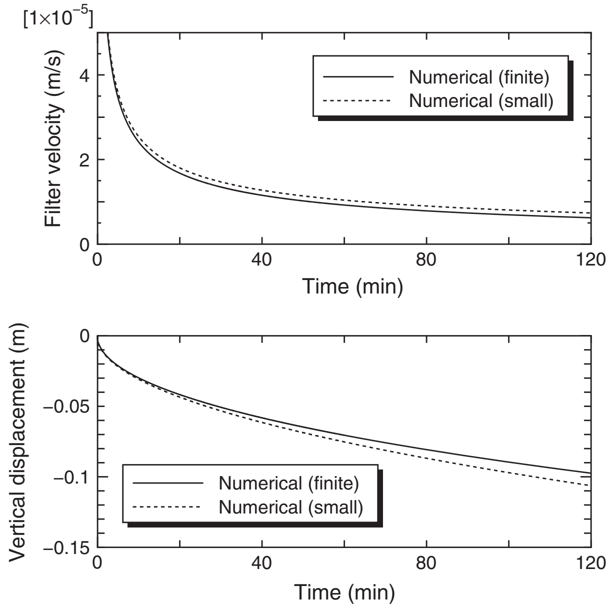

Figure 9. Time histories of leaking at the bottom of the soil specimen (top figure) and vertical displacement at the surface of the specimen (bottom figure) for Case 2.

deformation analyses of Case 2, the converged iteration number at each calculation step is seven times at the start and decreases to two times at the end of leaking.

4.3. Strip footing on unsaturated poroelastic material under harmonic loading

As a final example, we consider an unsaturated poroelastic deposit supporting a vertically vibrating strip footing. Some numerical conditions in this example are the same as those used in the analysis of fully saturated media [8] to verify the proposed method compared with the existing research and to show the difference between saturated and unsaturated behavior. Figure 10 shows the finite element model. The footing is 2 m wide, and the porous foundation block is 20 m wide and 10 m deep. The foundation is divided into 100 square eight-node elements. The left vertical boundary is the plane of symmetry, and hence, only the right half of the region is modeled. The time history of the footing load (in MPa) on the upper boundary is given by the function $w(t) = 3 - 3\cos(\omega t)$, where $\omega = 100$ rad/s is the circular frequency. The right and left boundaries are supported by vertical rollers, and the bottom boundary is supported by horizontal rollers. The upper boundary is free. As for pore air, the left and right boundaries are impermeable, while air drainage is allowed at the upper boundary. As for pore water, we consider the following cases in order to understand the effect of water saturation on the dynamic response.

Case 1. Fully saturated foundation. The initial water table is 0.0 m deep. Water drainage is allowed at the upper boundary in the static self-weight analyses and the dynamic analyses.
Case 2. Partially saturated foundation. The initial water table is 5.0 m deep, where the pore water pressure at the bottom boundary is 49 kPa in the static self-weight analyses. The upper and bottom boundaries are impermeable in the dynamic analyses.

Table III shows the material parameters for the two cases. In the dynamic analyses, the viscous damping of the solid skeleton is considered. In Case 2, the convergence of the calculation with VG model is not achieved; therefore, the LG model is used for the SWCC model in all cases. Figure 11 shows the SWCC and the relationship between the relative permeability of water and air and the effective degree of water saturation by the LG model. A time increment of calculation is 0.001 s in

DOI: 10.1002/nag

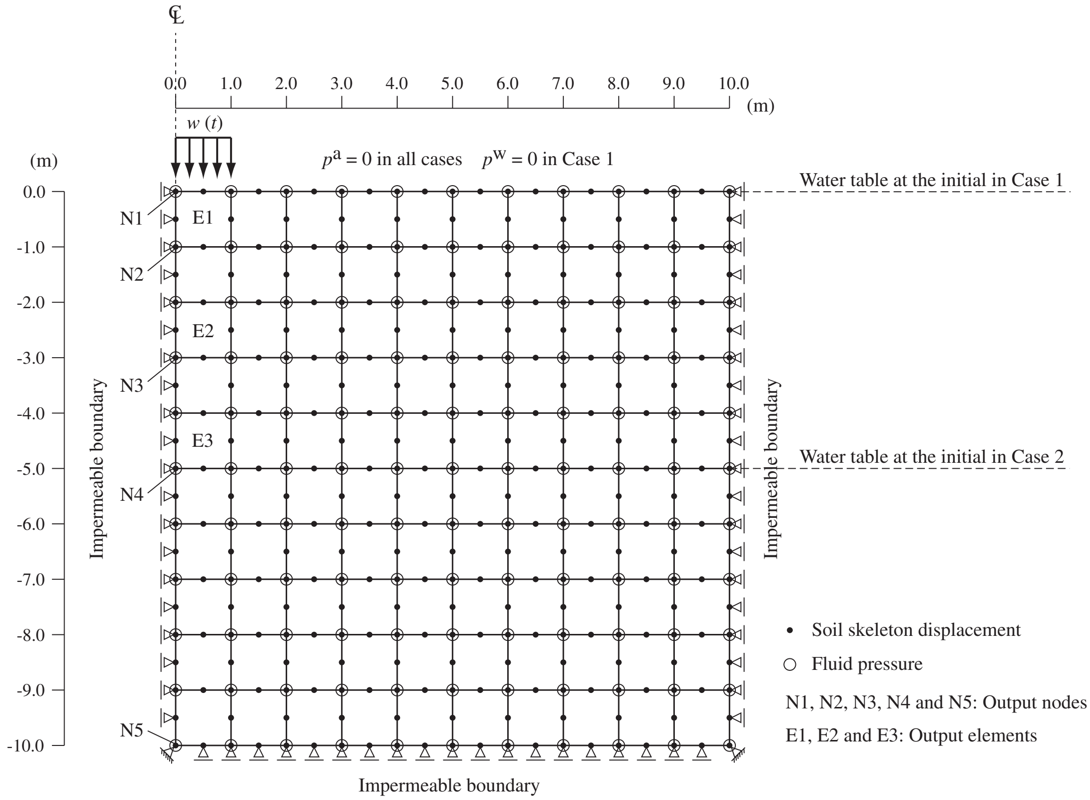

Figure 10. Finite element model in strip footing on unsaturated poroelastic material.

Table III. Material parameters in strip footing on unsaturated poroelastic material.

Parameter	Symbol	Case 1	Case 2
Intrinsic density of solid particle	ρ^{sR} (t/m^3)	2.6	2.6
Intrinsic density of pore water	ρ^{wR}_{0s} (t/m^3)	1.0	1.0
Intrinsic density of pore air	ρ^{aR}_{0s} (t/m^3)	-	1.2×10^{-3}
Initial porosity	n_{0s}	0.5	0.5
Saturated permeability coefficient of water	k^{ws}_{0s} (m/s)	1.0×10^{-3}	1.0×10^{-3}
Saturated permeability coefficient of air	k^{as}_{0s} (m/s)	-	1.0×10^{-4}
Bulk modulus of water	K^{w} (kN/m^2)	2.2×10^{6}	2.2×10^{6}
Air constant	$1/(\Theta\bar{R})(s^2/m^2)$	1.19×10^{-5}	1.19×10^{-5}
Minimum degree of water saturation	s^{w}_{r}	-	0.1
Maximum degree of water saturation	s^{w}_{s}	1.0	1.0
Parameters in LG model	a_{lg}	-	0.6
Parameters in LG model	b_{lg}	-	−6.0
Parameters in LG model	c_{lg}	-	0.1
Parameters in LG model	ξ_{lg}	-	3.0
Parameters in LG model	η_{lg}	-	1.5
Lamé constant	λ (kN/m^2)	6000.0	6000.0
Lamé constant	μ (kN/m^2)	4000.0	4000.0
Damping coefficient	α_{vis} (s)	0.02	0.02
Gravity force	g (m/s^2)	−9.8	−9.8

The subscript "0s" denotes the initial value in the reference configuration of solid skeleton.

dynamic analyses. The coefficient in Newmark integration method is $\gamma=0.6$ and $\beta=0.3025$. The error tolerance on the norm of residual vector is1.0×10^{-8}.

In all cases, the initial conditions are obtained with the static self-weight analyses under the above mentioned boundary conditions before carrying out the dynamic analyses with harmonic footing load.

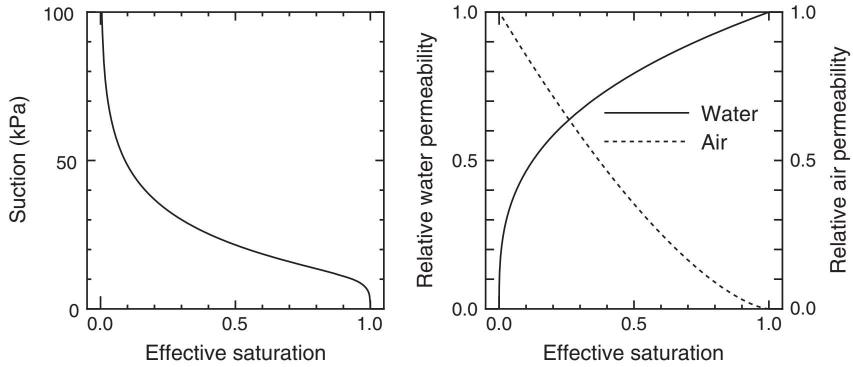

Figure 11. SWCC (left) and relative permeability (right) by LG model with the parameters in Table III.

Figure 12 shows the vertical distributions of pore water pressure and degree of water saturation at the initial state. The horizontal distributions of all variables are homogeneous at the initial condition. It is noted that the initial variables, such as pore water pressures at the same coordinates in the reference configuration, are slightly different between the finite deformation analyses and the small deformation analyses because of the settlement in the self-weight analyses. The vertical displacements at the surface in Cases 1 and 2 are 2.8 cm and 5.0 cm, respectively, after the self-weight analyses at finite strain.

First, the numerical results for Case 1 with fully saturated foundation are presented. Figure 13 shows the time histories of vertical displacements at node N1, which is located directly below the center of the footing (upper left corner node in Figure 10) and node N4, which is located at a depth of 5.0 m along the center line of the footing, in Case 1. The vertical displacement at node N1 fluctuates, and the peak time has a time lag for the harmonic loading history, while the vertical displacement at node N3 does not fluctuate. The amplitude of vertical displacement at node N4 is much smaller than that at node N1 although its change shows a similar perspective tendency as that at node N1. The amplitudes of vertical displacements predicted by the small deformation analyses are consistently larger than those predicted by the finite deformation analyses at the two nodes considered in Case 1. Figure 14 shows the time histories of pore water pressure at node N2, which is located at a depth of 1.0 m along the center line, and nodes N4 and N5, which are located at the bottom along the centerline of the footing (lower left corner node in Figure 10), in Case 1. The peak times of pore water pressures at all nodes correspond to the harmonic loading history. The amplitude of pore water pressure at node N2 is larger than that at nodes N3 and N4. The pore water pressure at node N2 reaches the maximum at about 0.03 s, and then, the peak amplitude gradually decreases because of the dissipation toward the drainage boundary. The amplitudes of the pore water pressure are higher for the finite deformation solutions than for the small deformation solutions at nodes N3 and N4 in Case 1. These results of the

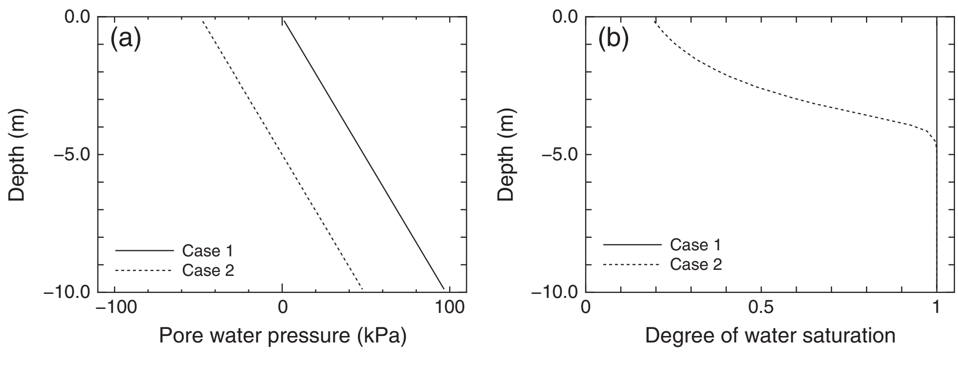

Figure 12. Vertical distributions of pore water pressure (left) and degree of water saturation (right) at the initial condition before harmonic loading.

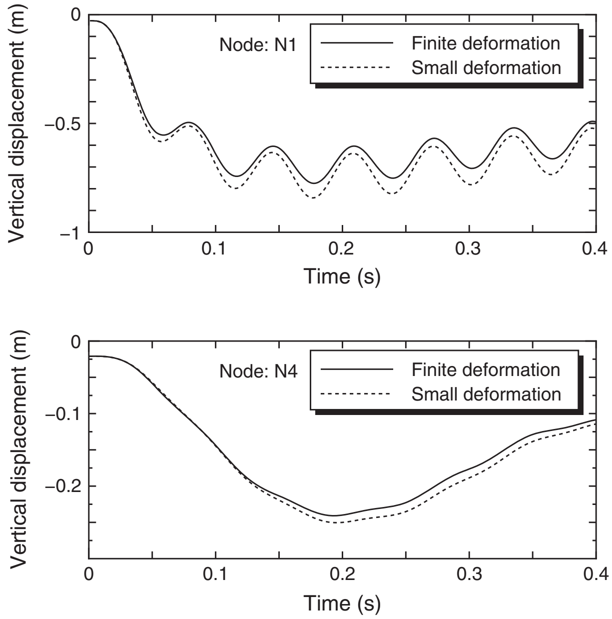

Figure 13. Time histories of vertical displacement at nodes N1 and N4 in Case 1.

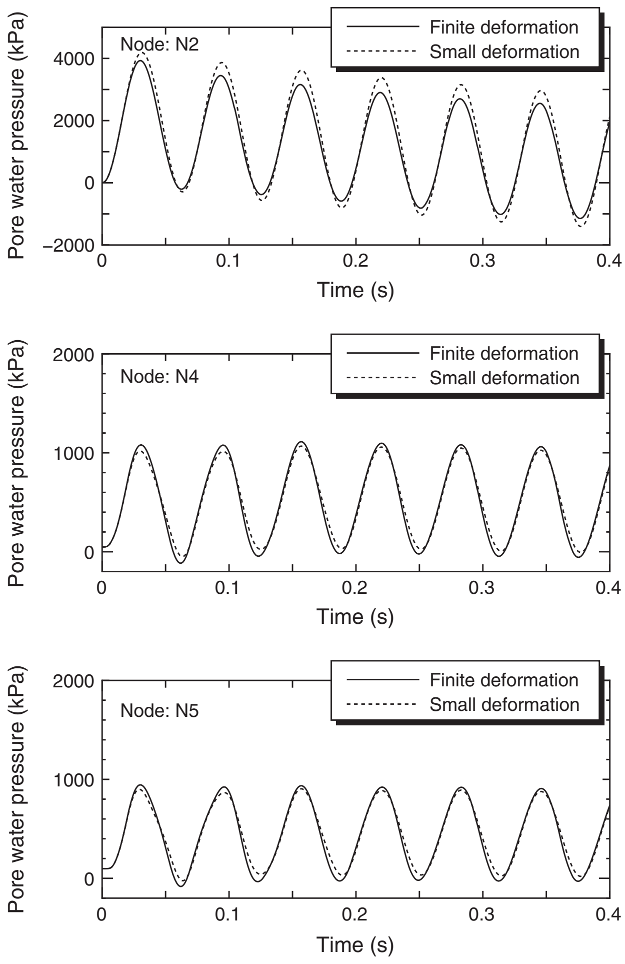

Figure 14. Time histories of pore water pressure at nodes N2, N4, and N5 in Case 1.

DOI: 10.1002/nag

displacements and pore water pressures are consistent with the two-phase dynamic analyses at finite strain [8]. Meanwhile, the amplitudes of the pore water pressure are smaller for the finite deformation solutions than for the small deformation solutions at nodes N2 in Case 1. Figure 15 shows the distributions of pore water pressure at 0.15 s when the peak pressures occur in Case 1. The higher pore water pressure is concentrated underneath the footing for both analyses. The maximum pore water pressure for the finite deformation analyses is smaller than that for the small deformation analyses underneath the footing, while the region with high pore water pressure for the finite deformation analysis is larger than that for the small deformation analysis.

Second, the numerical results in Case 2 with partially saturated foundation are presented. Figure 16 shows the time histories of vertical displacements at nodes N1 and N4 in Case 2. Although the results for Case 2 are similar to that for Case 1, the amplitude of vertical displacement at node N1 in Case 2 is much larger than that at node N1 in Case 1 because of higher compressibility of unsaturated

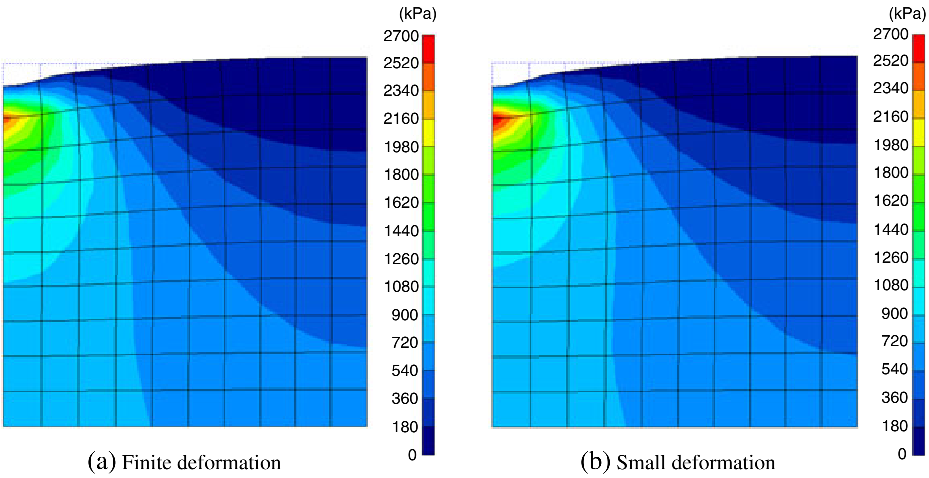

Figure 15. Distribution of pore water pressure at 0.15 s in Case 1.

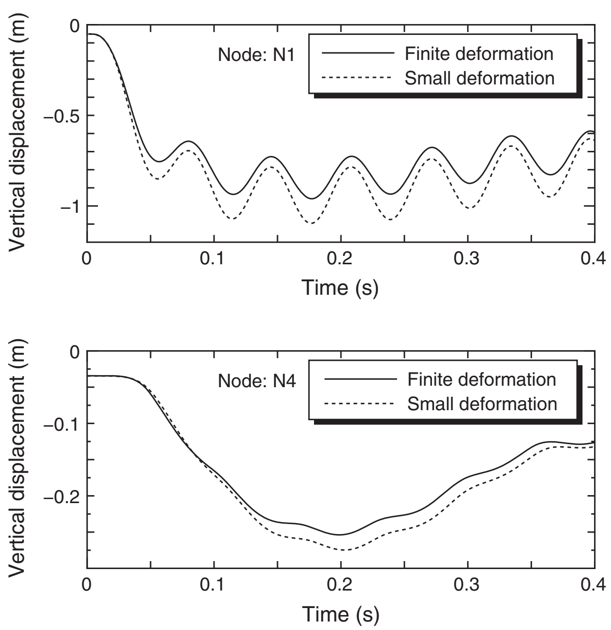

Figure 16. Time histories of vertical displacement at nodes N1 and N4 in Case 2.

DOI: 10.1002/nag

foundation above the water table. The amplitudes of vertical displacements predicted by the small deformation analyses are consistently larger than those predicted by the finite deformation analyses at two nodes similar to Case 1, and the difference between the two analyses in Case 2 is larger than that in Case 1. Figure 17 shows the time histories of pore water and air pressures of nodes N2, N3, and N4 in Case 2. The peak times of pore water and air pressures at all nodes have time lags for the harmonic loading history in contrast to Case 1. The pore air pressures fluctuate similar to pore water pressures. At nodes N2 and N3 in the unsaturated foundation, the amplitude of pore water and air pressures is much smaller than that at node N4 located near the water table. The pore water and air pressures at node N2 reaches the maximum at about 0.05 s, and then, the peak amplitude gradually decreases similar to Case 1. The wave forms at node N3 are different from those at nodes N2 and N4, and the phases of pore water and air pressures at node N3 are different by a phase shift value of about π from that at nodes N2 and N4. At node N4, which is located near the water table in the partially saturated foundation, the amplitude of pore water and pore air pressures reaches the maximum value at about 0.05 s, and then, the peak amplitude gradually decreases in contrast to Case 1. The amplitudes of the pore water and air pressure are higher for the finite deformation solutions than for the small deformation solutions at nodes N3 and N4, and vice versa, at node N2 similar to Case 1. However, the time histories of pore water and air pressures for the finite deformation analyses have a phase shift for that by the small deformation analyses at nodes N3 and N4 in contrast to Case 1. Figure 18 shows the distributions of pore water pressure at 0.175 s when the amplitude of vertical displacement at node N1 becomes the maximum in Case 2. The higher pore water pressure is concentrated underneath the water table around the depth of 5.0 m in the partially saturated foundation. In the unsaturated foundation underneath the footing, the region with high pore water pressure in the finite deformation analysis is smaller than that in the small deformation analysis, while the region with high pore water pressure in the finite deformation analysis is larger than that in the small deformation analysis below the water table in the fully saturated foundation, similar to Case 1.

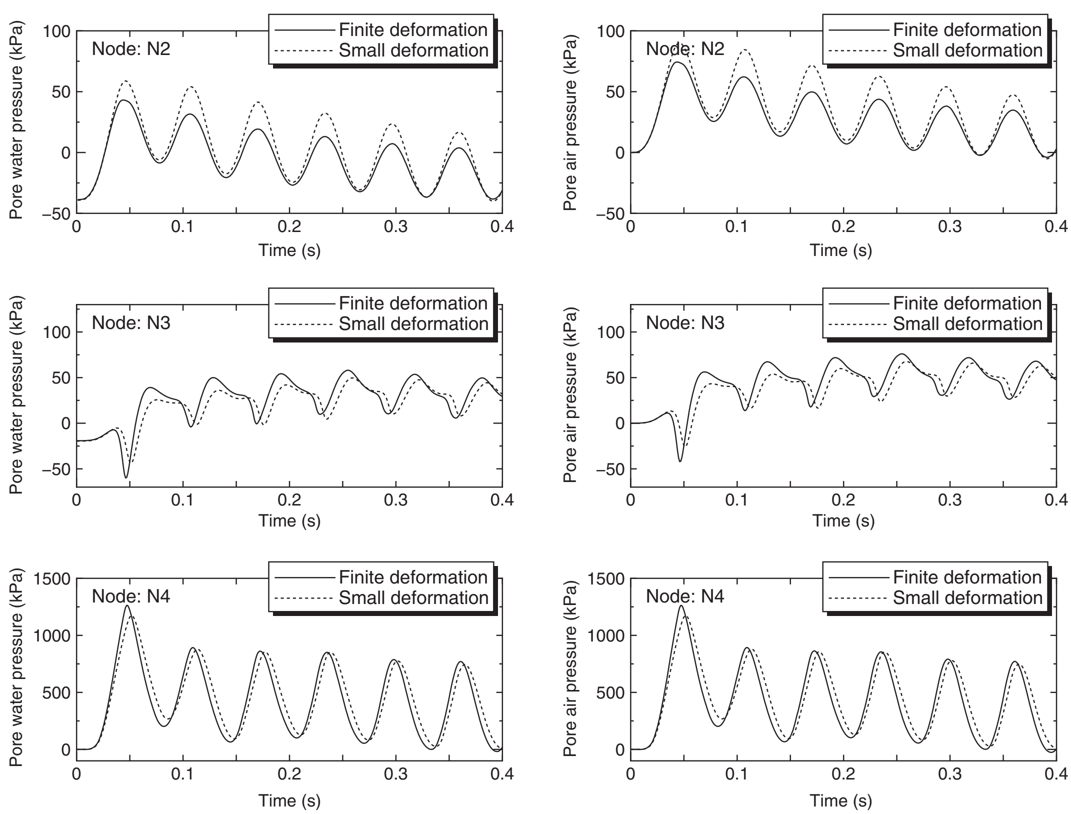

Figure 17. Time histories of pore water (left) and air pressures (right) at nodes N2, N3, and N4 in Case 2.

DOI: 10.1002/nag

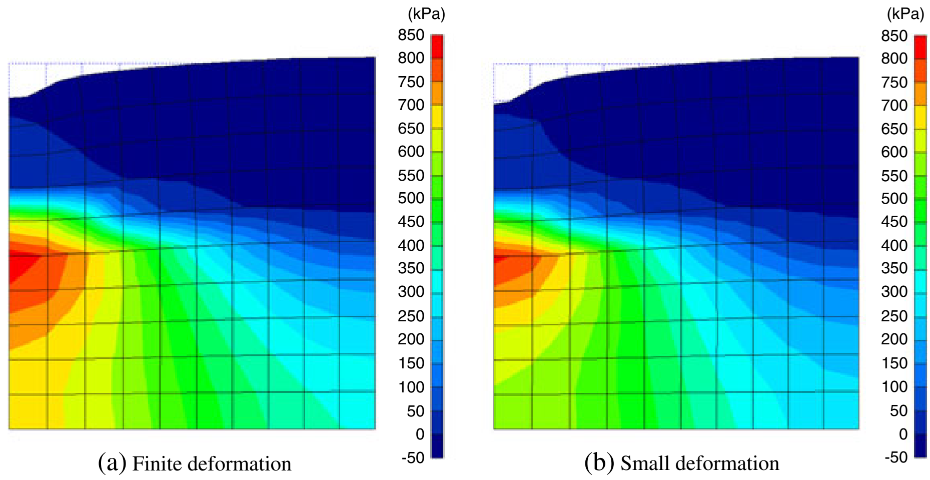

Figure 18. Distribution of pore water pressure at 0.175 s in Case 2.

Figure 19 shows the time histories of suction and water saturation at the central integration points at elements E1, E2, and E3 in Case 2. All output elements are located along the center line above the water table in Figure 10. The suctions in all elements decrease during the first loading and then fluctuate with the harmonic loading. Corresponding to the change in the suction, the water saturations increase at first and then fluctuate with the harmonic loading. The suction at all elements have almost the same phases with a phase shift of π for pore water and air pressure responses at node N2 and N4 in

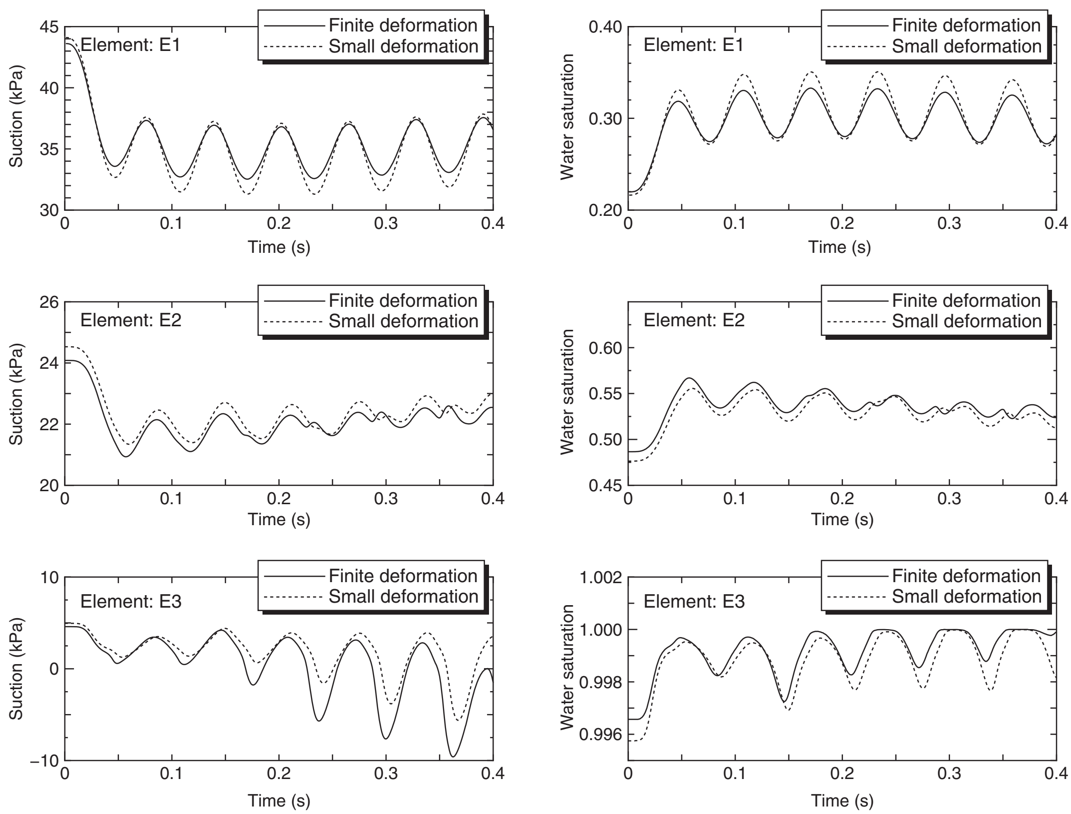

Figure 19. Time histories of suction (left) and water saturation (right) at elements E1, E2, and E3 in Case 2.

DOI: 10.1002/nag

Figure 17. At element E3, just above the water table, the amplitudes of fluctuation in suction gradually increase in contrast to elements E1 and E2 although the amplitudes of fluctuation in water saturation are very near to full saturation. The amplitudes of the suction and water saturation for element E1 are smaller for the finite deformation solutions than for the small deformation solutions similar to pore water and air pressure responses at node N2 in Figure 17. These differences are because of the different compressibility of the element E1 between the two analyses; thus, the compressibility in the small deformation analyses is overestimated to be higher than that in the finite deformation analyses. Meanwhile, the amplitudes of the suction and water saturation at element E2 are almost same in both finite and small deformation solutions in contrast to the responses at element E1. As the initial suction for the finite deformation analyses are slightly smaller than that for the small deformation analyses because of the settlement during the self-weight analyses, it is difficult to discuss the detailed comparison between the two analyses at elements E2 and E3. Figure 20 shows the distributions of water saturation at 0.175 s when the amplitude of vertical displacement at node N1 becomes the maximum in Case 2. The higher water saturation is observed along the center line below the footing. Although the finite deformation and small deformation analyses show similar distributions of saturation, the region with high water saturation in the small deformation analysis is larger than that in the finite deformation analysis underneath the footing.

We conclude this example by showing in Figure 21 the convergence profile exhibited by the Newton iterations for different time steps. The variable N shown in the figure is the number of

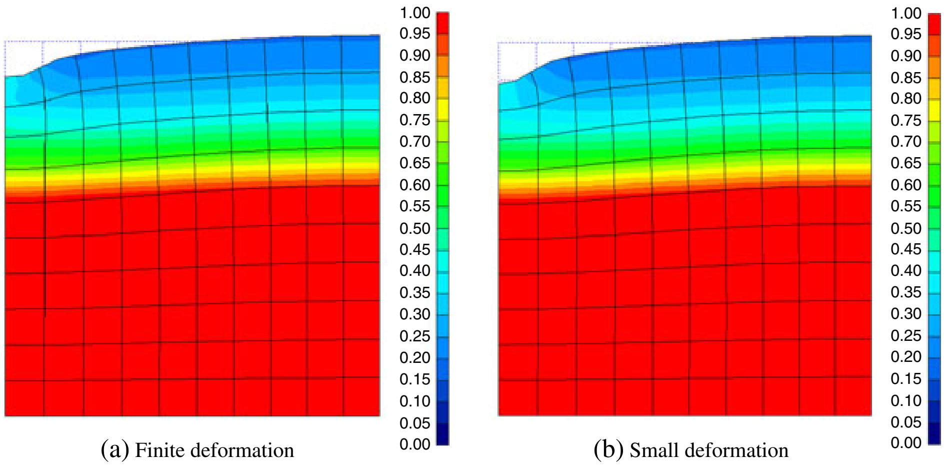

Figure 20. Distribution of water saturation at 0.175 s in Case 2.

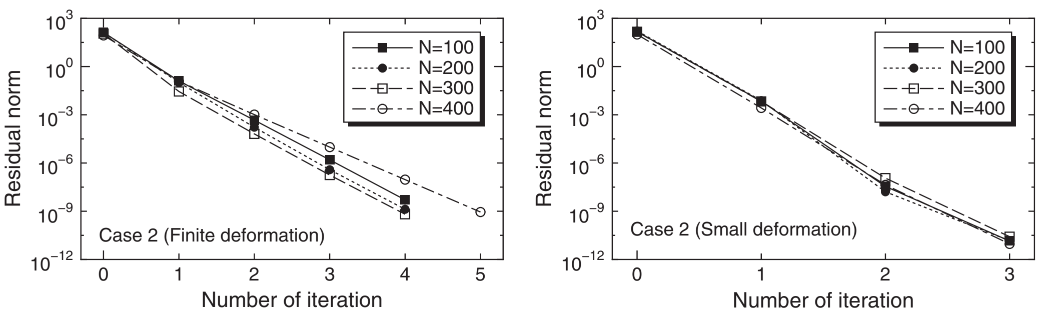

Figure 21. Convergence profile of global Newton iterations for finite deformation (left) and small deformation (right) analyses in Case 2.

DOI: 10.1002/nag

calculation step. We emphasize that the mixed formulation results in a tangent operator with a large condition number. However, with direct linear equation solving, convergence to an absolute error tolerance of 1.0×10^{-8} on the norm of the residual is very much possible in the finite and small deformation analyses. The convergence in the small deformation analyses with a smaller condition number is faster than that in the finite deformation analyses with a larger condition number. This performance illustrates the potential of the formulation and the iterative algorithm to accommodate more complex material constitutive models.

5. SUMMARY AND CONCLUSIONS

We have presented a coupled finite deformation formulation for the dynamic response of a mixture consisting of a poroelastic matrix and two types of fluid represented by water and air based on porous media theory. From the complete formulation, we have derived simplified equations by neglecting the material time derivative of relative velocities and the advection terms of the pore fluids relative to the solid matrix, leading to a so-called $u^{\mathrm{s}}-p^{\mathrm{w}}-p^{\mathrm{a}}$ formulation. The weak forms of the momentum and mass balance equations are implemented in a mixed finite element framework by imposing the conservation laws in the current configuration. The matrix equations are then linearized consistently and solved by Newton-Raphson iteration. A neo-Hookean hyperelastic model was used for the constitutive modeling of the solid skeleton based on a thermodynamically consistent measure of effective stress. Mass exchanges among phases were not considered in this paper.

Finite deformation and partial saturation influence the dynamic response of solid-water-air systems in a complex way. For example, the plane strain example involving a vibrating footing on a partially saturated poroelastic foundation discussed in this paper suggests that finite deformation effects tend to reduce the calculated pore water and pore air pressures under the footing. However, on a fully saturated poroelastic foundation, the reverse trend is true, i.e. finite deformation effects tend to increase the calculated pore water pressure responses. The vibrating footing example also shows that finite deformation and partial saturation impact the wave forms (amplitudes and phase shifts) of the pore water and pore air (for unsaturated foundation) pressure responses. Because the integrity of geotechnical structures is strongly influenced by the fluid pressure responses, the effects of finite deformation and partial saturation should be properly accounted for in the simulations.

This paper only considers a neo-Hookean hyperelastic material for constitutive modeling of the solid matrix response. The next step is to consider a more complex hyperelastic-plastic material. It is expected that hysteretic damping could further complicate the dynamic response of solid-water-air systems. It is for this reason that the present paper could serve as an important first step toward understanding the effect of finite deformation and partial saturation in the absence of plastic deformation and hysteretic damping. Plastic deformation and hysteretic damping will be addressed in a future publication. Work is also in progress to investigate the performance of a stabilized mixed finite element employing equal-order interpolation for the displacement and pore pressure fields in the regime of partial saturation [70].

APPENDIX A: LINEARIZATION OF WEAK FORMS

The details of the linearized weak forms in the current configuration are described here. It is convenient to linearize the weak forms transformed to the reference configuration by a pull-back operation because the initial volume dV^{s} in the reference configuration is constant during the linearization [4, 56, 59]. The linearized weak forms in the reference configuration then are transformed by a push-forward operation to the current configuration.

In the following, $\bar{c}$ is the derivative of specific soil moisture c with respect to suction p^{c}. $\bar{k}_{\mathrm{p}}^{\mathrm{ws}}$ is the derivative of pore water permeability k^{ws} with respect to suction p^{c}. $\bar{k}_{\mathrm{p}}^{\mathrm{as}}$ is the derivative of pore air permeability k^{as} with respect to suction p^{c}.

A.1. Momentum balance equation of total mixture

$$\delta w^{\mathrm{s}} = \delta w_1^{\mathrm{s}} + \delta w_2^{\mathrm{s}} + \delta w_3^{\mathrm{s}} + \delta w_4^{\mathrm{s}} + \delta w_5^{\mathrm{s}} \tag{A1}$$

$$\delta w_1^{\mathrm{s}} = \int_{B^{\mathrm{s}}} \rho \delta \boldsymbol{v}^{\mathrm{s}} \cdot \boldsymbol{a}^{\mathrm{s}} dv = \delta w_1^{\mathrm{s}}(\boldsymbol{a}^{\mathrm{s}}, \boldsymbol{u}^{\mathrm{s}}, p^{\mathrm{w}}, p^{\mathrm{a}}) \tag{A1a}$$

$$\delta w_2^{\mathrm{s}} = \int_{B^{\mathrm{s}}} \operatorname{grad} \delta \boldsymbol{v}^{\mathrm{s}} : \left(\boldsymbol{\sigma}'_{\mathrm{inv}} + \boldsymbol{\sigma}'_{\mathrm{vis}}\right) dv = \delta w_2^{\mathrm{s}}(\boldsymbol{u}^{\mathrm{s}}) \tag{A1b}$$

$$\delta w_3^{\mathrm{s}} = -\int_{B^{\mathrm{s}}} \bar{p} \operatorname{div} \delta \boldsymbol{v}^{\mathrm{s}} dv = \delta w_3^{\mathrm{s}}(\boldsymbol{u}^{\mathrm{s}}, p^{\mathrm{w}}, p^{\mathrm{a}}) \tag{A1c}$$

$$\delta w_4^{\mathrm{s}} = -\int_{B^{\mathrm{s}}} \rho \delta \boldsymbol{v}^{\mathrm{s}} \cdot \boldsymbol{b} dv = \delta w_4^{\mathrm{s}}(\boldsymbol{u}^{\mathrm{s}}, p^{\mathrm{w}}, p^{\mathrm{a}}) \tag{A1d}$$

$$\delta w_5^{\mathrm{s}} = -\int_{\partial B_{\mathrm{t}}^{\mathrm{s}}} \delta \boldsymbol{v}^{\mathrm{s}} \cdot \boldsymbol{t} da = \delta w_5^{\mathrm{s}}(t) \tag{A1e}$$

A.1.1. $D\delta w^{\mathrm{s}}[\Delta \boldsymbol{a}^{\mathrm{s}}]$.

$$D\delta w_1^{\mathrm{s}}[\Delta \boldsymbol{a}^{\mathrm{s}}] = \beta \Delta t^2 \int_{B^{\mathrm{s}}} \left(s^{\mathrm{w}} \rho^{\mathrm{wR}} + s^{\mathrm{a}} \rho^{\mathrm{aR}}\right) \delta \boldsymbol{v}^{\mathrm{s}} \cdot \boldsymbol{a}^{\mathrm{s}} \ \operatorname{div} \Delta \boldsymbol{a}^{\mathrm{s}} d\boldsymbol{v} + \int_{B^{\mathrm{s}}} \rho \delta \boldsymbol{v}^{\mathrm{s}} \cdot \Delta \boldsymbol{a}^{\mathrm{s}} dv \tag{A2}$$

$$\begin{aligned} D\delta w_2^{\mathrm{s}}[\Delta \boldsymbol{a}^{\mathrm{s}}] = {} & \beta \Delta t^2 \int_{B^{\mathrm{s}}} \left[\left\{ (\operatorname{grad} \Delta \boldsymbol{a}^{\mathrm{s}})^{\mathrm{T}} \operatorname{grad} \delta \boldsymbol{v}^{\mathrm{s}} \right\} : \boldsymbol{\sigma}' + \operatorname{sym}(\operatorname{grad} \delta \boldsymbol{v}^{\mathrm{s}}) : \boldsymbol{c} : \operatorname{sym}(\operatorname{grad} \Delta \boldsymbol{a}^{\mathrm{s}}) \right] dv \\ & + \int_{B^{\mathrm{s}}} \alpha_{\mathrm{vis}} \{ -\beta \Delta t^2 (\operatorname{grad} \delta \boldsymbol{v}^{\mathrm{s}} \ \operatorname{grad} \Delta \boldsymbol{a}^{\mathrm{s}}) : \boldsymbol{c} : \boldsymbol{d}^{\mathrm{s}} - 2\beta \Delta t^2 \frac{\lambda}{J^{\mathrm{s}}} \ \operatorname{div} \Delta \boldsymbol{a}^{\mathrm{s}} \operatorname{grad} \delta \boldsymbol{v}^{\mathrm{s}} : \boldsymbol{d}^{\mathrm{s}} \\ & + \gamma \Delta t \ \operatorname{grad} \delta \boldsymbol{v}^{\mathrm{s}} : \mathbf{c} : \operatorname{sym}(\operatorname{grad} \Delta \boldsymbol{a}^{\mathrm{s}}) - \beta \Delta t^2 \operatorname{grad} \delta \boldsymbol{v}^{\mathrm{s}} : \mathbf{c} : \operatorname{sym}(\operatorname{grad} \boldsymbol{v}^{\mathrm{s}} \ \operatorname{grad} \Delta \boldsymbol{a}^{\mathrm{s}}) \} dv \end{aligned} \tag{A3}$$

$$D\delta w_3^{\mathrm{s}}[\Delta \boldsymbol{a}^{\mathrm{s}}] = -\beta \Delta t^2 \int_{B^{\mathrm{s}}} \bar{p} \left\{ \operatorname{div} \Delta \boldsymbol{a}^{\mathrm{s}} \ \operatorname{div} \delta \boldsymbol{v}^{\mathrm{s}} - (\operatorname{grad} \delta \boldsymbol{v}^{\mathrm{s}})^{\mathrm{T}} : \ \operatorname{grad} \Delta \boldsymbol{a}^{\mathrm{s}} \right\} dv \tag{A4}$$

$$D\delta w_4^{\mathrm{s}}[\Delta \boldsymbol{a}^{\mathrm{s}}] = -\beta \Delta t^2 \int_{B^{\mathrm{s}}} \left(s^{\mathrm{w}} \rho^{\mathrm{wR}} + s^{\mathrm{a}} \rho^{\mathrm{aR}}\right) \delta \boldsymbol{v}^{\mathrm{s}} \cdot \boldsymbol{b} \ \operatorname{div} \Delta \boldsymbol{a}^{\mathrm{s}} dv \tag{A5}$$

$$D\delta w_5^{\mathrm{s}}[\Delta \boldsymbol{a}^{\mathrm{s}}] = 0 \tag{A6}$$

A.1.2. $D\delta w^{\mathrm{s}}[\Delta \ddot{p}^{\mathrm{w}}]$.

$$D\delta w_1^{\mathrm{s}}[\Delta \ddot{p}^{\mathrm{w}}] = \beta \Delta t^2 \int_{B^{\mathrm{s}}} n \left\{ \frac{s^{\mathrm{w}} \rho^{\mathrm{wR}}}{K^{\mathrm{w}}} + c\left(\rho^{\mathrm{aR}} - \rho^{\mathrm{wR}}\right) \right\} \delta \boldsymbol{v}^{\mathrm{s}} \cdot \boldsymbol{a}^{\mathrm{s}} \Delta \ddot{p}^{\mathrm{w}} dv \tag{A7}$$

$$D\delta w_2^{\mathrm{s}}[\Delta \ddot{p}^{\mathrm{w}}] = 0 \tag{A8}$$

DOI: 10.1002/nag

$$D\delta w_3^{\mathrm{s}}[\Delta\ddot{p}^{\mathrm{w}}] = -\beta\Delta t^2 \int_{B^{\mathrm{s}}} \{s^{\mathrm{w}} + c(p^{\mathrm{a}} - p^{\mathrm{w}})\}\ \operatorname{div}\delta\boldsymbol{v}^{\mathrm{s}}\Delta\ddot{p}^{\mathrm{w}} dv \tag{A9}$$

$$D\delta w_4^{\mathrm{s}}[\Delta\ddot{p}^{\mathrm{w}}] = -\beta\Delta t^2 \int_{B^{\mathrm{s}}} n\left\{\frac{s^{\mathrm{w}}\rho^{\mathrm{wR}}}{K^{\mathrm{w}}} + c(\rho^{\mathrm{aR}} - \rho^{\mathrm{wR}})\right\}\delta\boldsymbol{v}^{\mathrm{s}}\cdot\boldsymbol{b}\Delta\ddot{p}^{\mathrm{w}} dv \tag{A10}$$

$$D\delta w_5^{\mathrm{s}}[\Delta\ddot{p}^{\mathrm{w}}] = 0 \tag{A11}$$

A.1.3. $D\delta w^{\mathrm{s}}[\Delta\ddot{p}^{\mathrm{a}}]$.

$$\delta w_1^{\mathrm{s}}[\Delta\ddot{p}^{\mathrm{a}}] = \beta\Delta t^2 \int_{B^{\mathrm{s}}} n\left\{\frac{s^{\mathrm{a}}}{\Theta\bar{\bar{R}}} - c\left(\rho^{\mathrm{aR}} - \rho^{\mathrm{wR}}\right)\right\}\delta\boldsymbol{v}^{\mathrm{s}}\cdot\boldsymbol{a}^{\mathrm{s}}\Delta\ddot{p}^{\mathrm{a}} dv \tag{A12}$$

$$D\delta w_2^{\mathrm{s}}[\Delta\ddot{p}^{\mathrm{a}}] = 0 \tag{A13}$$

$$D\delta w_3^{\mathrm{s}}[\Delta\ddot{p}^{\mathrm{a}}] = -\beta\Delta t^2 \int_{B^{\mathrm{s}}} \{s^{\mathrm{a}} - c(p^{\mathrm{a}} - p^{\mathrm{w}})\}\ \operatorname{div}\delta\boldsymbol{v}^{\mathrm{s}}\Delta\ddot{p}^{\mathrm{a}} dv \tag{A14}$$

$$D\delta w_4^{\mathrm{s}}[\Delta\ddot{p}^{\mathrm{a}}] = -\beta\Delta t^2 \int_{B^{\mathrm{s}}} n\left\{\frac{s^{\mathrm{a}}}{\Theta\bar{R}} - c(\rho^{\mathrm{aR}} - \rho^{\mathrm{wR}})\right\}\delta\boldsymbol{v}^{\mathrm{s}}\cdot\boldsymbol{b}\Delta\ddot{p}^{\mathrm{a}} dv \tag{A15}$$

$$D\delta w_5^{\mathrm{s}}[\Delta\ddot{p}^{\mathrm{a}}] = 0 \tag{A16}$$

A.2. Mass and momentum balance equation of pore water

$$\delta w^{\mathrm{w}} = \delta w_1^{\mathrm{w}} + \delta w_2^{\mathrm{w}} + \delta w_3^{\mathrm{w}} + \delta w_4^{\mathrm{w}} + \delta w_5^{\mathrm{w}} + \delta w_6^{\mathrm{w}} + \delta w_7^{\mathrm{w}} \tag{A17}$$

$$\delta w_1^{\mathrm{w}} = \int_{B^{\mathrm{s}}} \delta p^{\mathrm{w}} n\left(\frac{s^{\mathrm{w}}\rho^{\mathrm{wR}}}{K^{\mathrm{w}}} - \rho^{\mathrm{wR}} c\right)\ \dot{p}^{\mathrm{w}} dv = \delta w_1^{\mathrm{w}}(\boldsymbol{u}^{\mathrm{s}}, p^{\mathrm{w}}, p^{\mathrm{a}}) \tag{A17a}$$

$$\delta w_2^{\mathrm{w}} = \int_{B^{\mathrm{s}}} \delta p^{\mathrm{w}} n\rho^{\mathrm{wR}} c\ \dot{p}^{\mathrm{a}} dv = \delta w_2^{\mathrm{w}}(\boldsymbol{u}^{\mathrm{s}}, p^{\mathrm{w}}, p^{\mathrm{a}}) \tag{A17b}$$

$$\delta w_3^{\mathrm{w}} = \int_{B^{\mathrm{s}}} \delta p^{\mathrm{w}} s^{\mathrm{w}} \rho^{\mathrm{wR}}\ \operatorname{div}\boldsymbol{v}^{\mathrm{s}} dv = \delta w_3^{\mathrm{w}}(\boldsymbol{u}^{\mathrm{s}}, p^{\mathrm{w}}, p^{\mathrm{a}}) \tag{A17c}$$

$$\delta w_4^{\mathrm{w}} = \int_{B^{\mathrm{s}}}\ \operatorname{grad}\delta p^{\mathrm{w}}\cdot\frac{k^{\mathrm{ws}}}{g}\ \operatorname{grad} p^{\mathrm{w}} dv = \delta w_4^{\mathrm{w}}(\boldsymbol{u}^{\mathrm{s}}, p^{\mathrm{w}}, p^{\mathrm{a}}) \tag{A17d}$$

$$\delta w_5^{\mathrm{w}} = -\int_{B^{\mathrm{s}}}\ \operatorname{grad}\delta p^{\mathrm{w}}\cdot\frac{k^{\mathrm{ws}}}{g}\rho^{\mathrm{wR}}\boldsymbol{b} dv = \delta w_5^{\mathrm{w}}(\boldsymbol{u}^{\mathrm{s}}, p^{\mathrm{w}}, p^{\mathrm{a}}) \tag{A17e}$$

$$\delta w_6^{\mathrm{w}} = \int_{B^{\mathrm{s}}}\ \operatorname{grad}\delta p^{\mathrm{w}}\cdot\frac{k^{\mathrm{ws}}}{g}\rho^{\mathrm{wR}}\boldsymbol{a}^{\mathrm{s}} dv = \delta w_6^{\mathrm{w}}(\boldsymbol{u}^{\mathrm{s}}, \boldsymbol{a}^{\mathrm{s}}, p^{\mathrm{w}}, p^{\mathrm{a}}) \tag{A17f}$$

$$\delta w_7^{\mathrm{w}} = \int_{\partial B^{\mathrm{s}}_{\mathrm{wq}}} \delta p^{\mathrm{w}} \overline{q}^{\mathrm{w}} da = \delta w_7^{\mathrm{w}}(t) \tag{A17g}$$

A.2.1. $D\delta w^{\mathrm{w}}[\Delta \boldsymbol{a}^{\mathrm{s}}]$.

$$D\delta w_1^{\mathrm{w}}[\Delta \boldsymbol{a}^{\mathrm{s}}] = \beta \Delta t^2 \int_{B^{\mathrm{s}}} \delta p^{\mathrm{w}} \rho^{\mathrm{wR}} \left(\frac{s^{\mathrm{w}}}{K^{\mathrm{w}}} - c \right) \dot{p}^{\mathrm{w}} \; \mathrm{div}\, \Delta \boldsymbol{a}^{\mathrm{s}} dv \tag{A18}$$

$$D\delta w_2^{\mathrm{w}}[\Delta \boldsymbol{a}^{\mathrm{s}}] = \beta \Delta t^2 \int_{B^{\mathrm{s}}} \delta p^{\mathrm{w}} \rho^{\mathrm{wR}} c \; \dot{p}^{\mathrm{a}} \; \mathrm{div}\, \Delta \boldsymbol{a}^{\mathrm{s}} dv \tag{A19}$$

$$\begin{aligned} D\delta w_2^{\mathrm{w}}[\Delta \boldsymbol{a}^{\mathrm{s}}] &= \beta \Delta t^2 \int_{B^{\mathrm{s}}} \delta p^{\mathrm{w}} \rho^{\mathrm{wR}} c \; \dot{p}^{\mathrm{a}} \; \mathrm{div}\, \Delta \boldsymbol{a}^{\mathrm{s}} dv \\ &+ \beta \Delta t^2 \int_{B^{\mathrm{s}}} \delta p^{\mathrm{w}} s^{\mathrm{w}} \rho^{\mathrm{wR}} \left\{ \mathrm{div}\, \boldsymbol{v}^{\mathrm{s}} \; \mathrm{div}\, \Delta \boldsymbol{a}^{\mathrm{s}} - (\mathrm{grad}\, \boldsymbol{v}^{\mathrm{s}})^{\mathrm{T}} : \; \mathrm{grad}\, \Delta \boldsymbol{a}^{\mathrm{s}} \right\} dv \end{aligned} \tag{A20}$$

$$\begin{aligned} D\delta w_4^{\mathrm{w}}[\Delta \boldsymbol{a}^{\mathrm{s}}] = \frac{1}{g} \beta \Delta t^2 \int_{B^{\mathrm{s}}} k^{\mathrm{ws}} \Big[&-2\, \mathrm{grad}\, \delta p^{\mathrm{w}} \cdot \{ \mathrm{sym}(\mathrm{grad}\, \Delta \boldsymbol{a}^{\mathrm{s}})\, \mathrm{grad}\, p^{\mathrm{w}} \} \\ &+ \mathrm{grad}\, \delta p^{\mathrm{w}} \cdot \; \mathrm{grad}\, p^{\mathrm{w}}\, \mathrm{div} \Delta \boldsymbol{a}^{\mathrm{s}} \Big] dv \end{aligned} \tag{A21}$$

$$D\delta w_5^{\mathrm{w}}[\Delta \boldsymbol{a}^{\mathrm{s}}] = -\frac{1}{g} \beta \Delta t^2 \int_{B^{\mathrm{s}}} k^{\mathrm{ws}} \rho^{\mathrm{wR}} \left\{ - \; \mathrm{grad}\, \delta p^{\mathrm{w}} \cdot (\; \mathrm{grad}\, \Delta \boldsymbol{a}^{\mathrm{s}}\, \boldsymbol{b}) + \; \mathrm{grad}\, \delta p^{\mathrm{w}} \cdot \boldsymbol{b} \; \mathrm{div}\, \Delta \boldsymbol{a}^{\mathrm{s}} \right\} dv \tag{A22}$$

$$\begin{aligned} D\delta w_6^{\mathrm{w}}[\Delta \boldsymbol{a}^{\mathrm{s}}] = &\frac{1}{g} \int_{B^{\mathrm{s}}} k^{\mathrm{ws}} \rho^{\mathrm{wR}} \; \mathrm{grad}\, \delta p^{\mathrm{w}} \cdot \Delta \boldsymbol{a}^{\mathrm{s}} dv \\ &+ \frac{1}{g} \beta \Delta t^2 \int_{B^{\mathrm{s}}} k^{\mathrm{ws}} \rho^{\mathrm{wR}} \{ - \; \mathrm{grad}\, \delta p^{\mathrm{w}} \cdot (\; \mathrm{grad}\, \Delta \boldsymbol{a}^{\mathrm{s}} \boldsymbol{a}^{\mathrm{s}}) + \mathrm{grad}\, \delta p^{\mathrm{w}} \cdot \boldsymbol{a}^{\mathrm{s}} \; \mathrm{div}\, \Delta \boldsymbol{a}^{\mathrm{s}} \} dv \end{aligned} \tag{A23}$$

$$D\delta w_7^{\mathrm{w}}[\Delta \boldsymbol{a}^{\mathrm{s}}] = 0 \tag{A24}$$

A.2.2. $D\delta w^{\mathrm{w}}[\Delta \ddot{p}^{\mathrm{w}}]$.

$$\begin{aligned} D\delta w_1^{\mathrm{w}}[\Delta \ddot{p}^{\mathrm{w}}] = &\beta \Delta t^2 \int_{B^{\mathrm{s}}} \delta p^{\mathrm{w}} n \rho^{\mathrm{wR}} \left\{ \frac{s^{\mathrm{w}}}{(K^{\mathrm{w}})^2} - 2 \frac{c}{K^{\mathrm{w}}} + \overline{c} \right\} \dot{p}^{\mathrm{w}} \Delta \ddot{p}^{\mathrm{w}} dv \\ &+ \gamma \Delta t \int_{B^{\mathrm{s}}} \delta p^{\mathrm{w}} n \rho^{\mathrm{wR}} \left(\frac{s^{\mathrm{w}}}{K^{\mathrm{w}}} - c \right) \Delta \ddot{p}^{\mathrm{w}} dv \end{aligned} \tag{A25}$$

$$D\delta w_2^{\mathrm{w}}[\Delta \ddot{p}^{\mathrm{w}}] = \beta \Delta t^2 \int_{B^{\mathrm{s}}} \delta p^{\mathrm{w}} n \rho^{\mathrm{wR}} \left(\frac{c}{K^{\mathrm{w}}} - \overline{c} \right) \Delta \ddot{p}^{\mathrm{w}} \; \dot{p}^{\mathrm{a}} dv \tag{A26}$$

$$D\delta w_3^{\mathrm{w}}[\Delta \ddot{p}^{\mathrm{w}}] = \beta \Delta t^2 \int_{B^{\mathrm{s}}} \delta p^{\mathrm{w}} \left(-c \rho^{\mathrm{wR}} + \frac{s^{\mathrm{w}} \rho^{\mathrm{wR}}}{K^{\mathrm{w}}} \right) \mathrm{div}\, \boldsymbol{v}^{\mathrm{s}} \Delta \ddot{p}^{\mathrm{w}} dv \tag{A27}$$

$$D\delta w_4^{\mathrm{w}}[\Delta \ddot{p}^{\mathrm{w}}] = \frac{1}{g} \beta \Delta t^2 \int_{B^{\mathrm{s}}} \; \mathrm{grad} \; \delta p^{\mathrm{w}} \cdot \left(-\mathrm{grad}\, p^{\mathrm{w}} \overline{k}_{\mathrm{p}}^{\mathrm{ws}} \Delta \ddot{p}^{\mathrm{w}} + \; \mathrm{grad}\, \Delta \ddot{p}^{\mathrm{w}} k^{\mathrm{ws}} \right) dv \tag{A28}$$

$$D\delta w_5^{\mathrm{w}}[\Delta\ddot{p}^{\mathrm{w}}] = -\frac{1}{g}\beta\Delta t^2 \int_{B^{\mathrm{s}}} \operatorname{grad}\delta p^{\mathrm{w}} \cdot \boldsymbol{b}\left(-\overline{k}_{\mathrm{p}}^{\mathrm{ws}}\rho^{\mathrm{wR}} + k^{\mathrm{ws}}\frac{\rho^{\mathrm{wR}}}{K^{\mathrm{w}}}\right)\Delta\ddot{p}^{\mathrm{w}} dv \tag{A29}$$

$$D\delta w_6^{\mathrm{w}}[\Delta\ddot{p}^{\mathrm{w}}] = \frac{1}{g}\beta\Delta t^2 \int_{B^{\mathrm{s}}} \operatorname{grad}\delta p^{\mathrm{w}} \cdot \boldsymbol{a}^{\mathrm{s}}\left(-\overline{k}_{\mathrm{p}}^{\mathrm{ws}}\rho^{\mathrm{wR}} + k^{\mathrm{ws}}\frac{\rho^{\mathrm{wR}}}{K^{\mathrm{w}}}\right)\Delta\ddot{p}^{\mathrm{w}} dv \tag{A30}$$

$$D\delta w_7^{\mathrm{w}}[\Delta\ddot{p}^{\mathrm{w}}] = 0 \tag{A31}$$

A.2.3. $D\delta w^{\mathrm{w}}[\Delta\ddot{p}^{\mathrm{a}}]$.

$$D\delta w_1^{\mathrm{w}}[\Delta\ddot{p}^{\mathrm{a}}] = \beta\Delta t^2 \int_{B^{\mathrm{s}}} \delta p^{\mathrm{w}} n\rho^{\mathrm{wR}}\left(\frac{c}{K^{\mathrm{w}}} - \overline{c}\right)\dot{p}^{\mathrm{w}}\Delta\ddot{p}^{\mathrm{a}} dv \tag{A32}$$

$$D\delta w_2^{\mathrm{w}}[\Delta\ddot{p}^{\mathrm{a}}] = \beta\Delta t^2 \int_{B^{\mathrm{s}}} \delta p^{\mathrm{w}} n\rho^{\mathrm{wR}}\overline{c}\,\dot{p}^{\mathrm{a}}\Delta\ddot{p}^{\mathrm{a}} dv + \gamma\Delta t \int_{B^{\mathrm{s}}} \delta p^{\mathrm{w}} n\rho^{\mathrm{wR}} c\Delta\ddot{p}^{\mathrm{a}} dv \tag{A33}$$

$$D\delta w_3^{\mathrm{w}}[\Delta\ddot{p}^{\mathrm{a}}] = \beta\Delta t^2 \int_{B^{\mathrm{s}}} \delta p^{\mathrm{w}}\rho^{\mathrm{wR}} c \operatorname{div}\boldsymbol{v}^{\mathrm{s}}\Delta\ddot{p}^{\mathrm{a}} dv \tag{A34}$$

$$D\delta w_4^{\mathrm{w}}[\Delta\ddot{p}^{\mathrm{a}}] = \frac{1}{g}\beta\Delta t^2 \int_{B^{\mathrm{s}}} \operatorname{grad}\delta p^{\mathrm{w}} \cdot \operatorname{grad} p^{\mathrm{w}}\, \overline{k}_{\mathrm{p}}^{\mathrm{ws}}\Delta\ddot{p}^{\mathrm{a}} dv \tag{A35}$$

$$D\delta w_5^{\mathrm{w}}[\Delta\ddot{p}^{\mathrm{a}}] = -\frac{1}{g}\beta\Delta t^2 \int_{B^{\mathrm{s}}} \operatorname{grad}\delta p^{\mathrm{w}} \cdot \boldsymbol{b}\overline{k}_{\mathrm{p}}^{\mathrm{ws}}\rho^{\mathrm{wR}}\Delta\ddot{p}^{\mathrm{a}} dv \tag{A36}$$

$$D\delta w_6^{\mathrm{w}}[\Delta\ddot{p}^{\mathrm{a}}] = \frac{1}{g}\beta\Delta t^2 \int_{B^{\mathrm{s}}} \operatorname{grad}\delta p^{\mathrm{w}} \cdot \boldsymbol{a}^{\mathrm{s}}\, \overline{k}_{\mathrm{p}}^{\mathrm{ws}}\rho^{\mathrm{wR}}\Delta\ddot{p}^{\mathrm{a}} dv \tag{A37}$$

$$D\delta w_7^{\mathrm{w}}[\Delta\ddot{p}^{\mathrm{a}}] = 0 \tag{A38}$$

A.3. Mass and momentum balance equation of pore air

$$\delta w^{\mathrm{a}} = \delta w_1^{\mathrm{a}} + \delta w_2^{\mathrm{a}} + \delta w_3^{\mathrm{a}} + \delta w_4^{\mathrm{a}} + \delta w_5^{\mathrm{a}} + \delta w_6^{\mathrm{a}} + \delta w_7^{\mathrm{a}} \tag{A39}$$

$$\delta w_1^{\mathrm{a}} = \int \delta p^{\mathrm{a}} n\left\{\frac{(1-s^{\mathrm{w}})}{\Theta\overline{R}} - \rho^{\mathrm{aR}} c\right\}\dot{p}^{\mathrm{a}} dv = \delta w_1^{\mathrm{a}}(\boldsymbol{u}^{\mathrm{s}}, p^{\mathrm{w}}, p^{\mathrm{a}}) \tag{A39a}$$

$$\delta w_2^{\mathrm{a}} = \int_{B^{\mathrm{s}}} \delta p^{\mathrm{a}}\rho^{\mathrm{aR}} c\,\dot{p}^{\mathrm{w}} dv = \delta w_2^{\mathrm{a}}(\boldsymbol{u}^{\mathrm{s}}, p^{\mathrm{w}}, p^{\mathrm{a}}) \tag{A39b}$$

$$\delta w_3^{\mathrm{a}} = \int_{B^{\mathrm{s}}} \delta p^{\mathrm{a}}(1-s^{\mathrm{w}})\rho^{\mathrm{aR}} \operatorname{div}\boldsymbol{v}^{\mathrm{s}} dv = \delta w_3^{\mathrm{a}}(\boldsymbol{u}^{\mathrm{s}}, p^{\mathrm{w}}, p^{\mathrm{a}}) \tag{A39c}$$

DOI: 10.1002/nag

$$\delta w_4^{\mathrm{a}} = \int_{B^{\mathrm{s}}} \frac{k^{\mathrm{as}}}{g} \ \mathrm{grad}\,\delta p^{\mathrm{a}} \cdot \ \mathrm{grad}\, p^{\mathrm{a}} dv = \delta w_4^{\mathrm{a}}(\boldsymbol{u}^{\mathrm{s}}, p^{\mathrm{w}}, p^{\mathrm{a}}) \tag{A39d}$$

$$\delta w_5^{\mathrm{a}} = -\int_{B^{\mathrm{s}}} \frac{k^{\mathrm{as}}}{g} \rho^{\mathrm{aR}} \ \mathrm{grad}\,\delta p^{\mathrm{a}} \cdot \boldsymbol{b} dv = \delta w_5^{\mathrm{a}}(\boldsymbol{u}^{\mathrm{s}}, p^{\mathrm{w}}, p^{\mathrm{a}}) \tag{A39e}$$

$$\delta w_6^{\mathrm{a}} = \int_{B^{\mathrm{s}}} \frac{k^{\mathrm{as}}}{g} \rho^{\mathrm{aR}} \ \mathrm{grad}\,\delta p^{\mathrm{a}} \cdot \boldsymbol{a}^{\mathrm{s}} dv = \delta w_6^{\mathrm{a}}(\boldsymbol{u}^{\mathrm{s}}, \boldsymbol{a}^{\mathrm{s}}, p^{\mathrm{w}}, p^{\mathrm{a}}) \tag{A39f}$$

$$\delta w_7^{\mathrm{a}} = \int_{\partial B^{\mathrm{s}}_{\mathrm{aq}}} \delta p^{\mathrm{a}} \overline{q}^{\mathrm{a}} da = \delta w_7^{\mathrm{a}}(t) \tag{A39g}$$

A.3.1. $D\delta w^{\mathrm{a}}[\Delta \boldsymbol{a}^{\mathrm{s}}]$.

$$D\delta w_1^{\mathrm{a}}[\Delta \boldsymbol{a}^{\mathrm{s}}] = \beta \Delta t^2 \int_{B^{\mathrm{s}}} \delta p^{\mathrm{a}} \left\{ \frac{(1-s^{\mathrm{w}})}{\Theta \overline{R}} - \rho^{\mathrm{aR}} c \right\} \dot{p}^{\mathrm{a}} \ \mathrm{div}\,\Delta \boldsymbol{a}^{\mathrm{s}} dv \tag{A40}$$

$$D\delta w_2^{\mathrm{a}}[\Delta \boldsymbol{a}^{\mathrm{s}}] = \beta \Delta t^2 \int_{B^{\mathrm{s}}} \delta p^{\mathrm{a}} \rho^{\mathrm{aR}} c \ \dot{p}^{\mathrm{w}} \ \mathrm{div}\,\Delta \boldsymbol{a}^{\mathrm{s}} dv \tag{A41}$$

$$\begin{aligned} D\delta w_3^{\mathrm{a}}[\Delta \boldsymbol{a}^{\mathrm{s}}] &= \gamma \Delta t \int_{B^{\mathrm{s}}} \delta p^{\mathrm{a}} (1-s^{\mathrm{w}}) \rho^{\mathrm{aR}} \ \mathrm{div}\,\Delta \boldsymbol{a}^{\mathrm{s}} dv \\ &+ \beta \Delta t^2 \int_{B^{\mathrm{s}}} \delta p^{\mathrm{a}} (1-s^{\mathrm{w}}) \rho^{\mathrm{aR}} \left\{ \mathrm{div}\,\boldsymbol{v}^{\mathrm{s}} \ \mathrm{div}\,\Delta \boldsymbol{a}^{\mathrm{s}} - (\mathrm{grad}\,\boldsymbol{v}^{\mathrm{s}})^{\mathrm{T}} : \ \mathrm{grad}\,\Delta \boldsymbol{a}^{\mathrm{s}} \right\} dv \end{aligned} \tag{A42}$$

$$\begin{aligned} D\delta w_4^{\mathrm{a}}[\Delta \boldsymbol{a}^{\mathrm{s}}] = \frac{1}{g} \beta \Delta t^2 \int_{B^{\mathrm{s}}} k^{\mathrm{as}} \Big[&-2 \ \mathrm{grad}\,\delta p^{\mathrm{a}} \cdot \{ \mathrm{sym}(\ \mathrm{grad}\,\Delta \boldsymbol{a}^{\mathrm{s}}) \ \mathrm{grad}\, p^{\mathrm{a}} \} \\ &+ \ \mathrm{grad}\,\delta p^{\mathrm{a}} \cdot \ \mathrm{grad}\, p^{\mathrm{a}} \ \mathrm{div}\,\Delta \boldsymbol{a}^{\mathrm{s}} \Big] dv \end{aligned} \tag{A43}$$

$$D\delta w_5^{\mathrm{a}}[\Delta \boldsymbol{a}^{\mathrm{s}}] = -\frac{1}{g} \beta \Delta t^2 \int_{B^{\mathrm{s}}} k^{\mathrm{as}} \rho^{\mathrm{aR}} \left\{ -\mathrm{grad} \ \delta p^{\mathrm{a}} \cdot (\mathrm{grad}\,\Delta \boldsymbol{a}^{\mathrm{s}} \boldsymbol{b}) + \mathrm{grad} \ \delta p^{\mathrm{a}} \cdot \boldsymbol{b} \ \mathrm{div}\,\Delta \boldsymbol{a}^{\mathrm{s}} \right\} dv \tag{A44}$$

$$\begin{aligned} D\delta w_6^{\mathrm{a}}[\Delta \boldsymbol{a}^{\mathrm{s}}] = &\frac{1}{g} \int_{B^{\mathrm{s}}} k^{\mathrm{as}} \rho^{\mathrm{aR}} \ \mathrm{grad}\,\delta p^{\mathrm{a}} \cdot \Delta \boldsymbol{a}^{\mathrm{s}} dv \\ &+ \frac{1}{g} \beta \Delta t^2 \int_{B^{\mathrm{s}}} k^{\mathrm{as}} \rho^{\mathrm{aR}} \{ - \ \mathrm{grad}\,\delta p^{\mathrm{a}} \cdot (\ \mathrm{grad}\,\Delta \boldsymbol{a}^{\mathrm{s}} \ \boldsymbol{a}^{\mathrm{s}}) + \ \mathrm{grad}\,\delta p^{\mathrm{a}} \cdot \boldsymbol{a}^{\mathrm{s}} \ \mathrm{div}\,\Delta \boldsymbol{a}^{\mathrm{s}} \} dv \end{aligned} \tag{A45}$$

$$D\delta w_7^{\mathrm{a}}[\Delta \boldsymbol{a}^{\mathrm{s}}] = 0 \tag{A46}$$

A.3.2. $D\delta w^{\mathrm{a}}[\Delta \ddot{p}^{\mathrm{w}}]$.

$$D\delta w_1^{\mathrm{a}}[\Delta \ddot{p}^{\mathrm{w}}] = \beta \Delta t^2 \int_{B^{\mathrm{s}}} \delta p^{\mathrm{a}} n \left(\frac{1}{\Theta \overline{R}} c + \rho^{\mathrm{aR}} \overline{c} \right) \ \dot{p}^{\mathrm{a}} \Delta \ddot{p}^{\mathrm{w}} dv \tag{A47}$$

DOI: 10.1002/nag

$$D\delta w_2^{\mathrm{a}}[\Delta \ddot{p}^{\mathrm{w}}] = -\beta\Delta t^2 \int_{B^{\mathrm{s}}} \delta p^{\mathrm{a}} n \rho^{\mathrm{aR}} \overline{c}\, \dot{p}^{\mathrm{w}} \Delta \ddot{p}^{\mathrm{w}} dv + \gamma\Delta t \int_{B^{\mathrm{s}}} \delta p^{\mathrm{a}} n \rho^{\mathrm{aR}} c \Delta \ddot{p}^{\mathrm{w}} dv \tag{A48}$$

$$D\delta w_3^{\mathrm{a}}[\Delta \ddot{p}^{\mathrm{w}}] = \beta\Delta t^2 \int_{B^{\mathrm{s}}} \delta p^{\mathrm{a}} \rho^{\mathrm{aR}} c \;\mathrm{div}\, \boldsymbol{v}^{\mathrm{s}} \Delta \ddot{p}^{\mathrm{w}} dv \tag{A49}$$

$$\delta w_4^{\mathrm{a}}[\Delta \ddot{p}^{\mathrm{w}}] = -\frac{1}{g}\beta\Delta t^2 \int_{B^{\mathrm{s}}} \mathrm{grad}\, \delta p^{\mathrm{a}} \cdot \;\mathrm{grad}\, p^{\mathrm{a}}\, \overline{k}_{\mathrm{p}}^{\mathrm{as}} \Delta \ddot{p}^{\mathrm{w}} dv \tag{A50}$$

$$D\delta w_5^{\mathrm{a}}[\Delta \ddot{p}^{\mathrm{w}}] = \frac{1}{g}\beta\Delta t^2 \int_{B^{\mathrm{s}}} \mathrm{grad}\, \delta p^{\mathrm{a}} \cdot \boldsymbol{b}\, \overline{k}_{\mathrm{p}}^{\mathrm{as}} \rho^{\mathrm{aR}} \Delta \ddot{p}^{\mathrm{w}} dv \tag{A51}$$

$$D\delta w_6^{\mathrm{a}}[\Delta \ddot{p}^{\mathrm{w}}] = -\frac{1}{g}\beta\Delta t^2 \int_{B^{\mathrm{s}}} \mathrm{grad}\, \delta p^{\mathrm{a}} \cdot \boldsymbol{a}^{\mathrm{s}}\; \overline{k}_{\mathrm{p}}^{\mathrm{as}} \rho^{\mathrm{aR}} \Delta \ddot{p}^{\mathrm{w}} dv \tag{A52}$$

$$\delta w_7^{\mathrm{a}}[\Delta \ddot{p}^{\mathrm{w}}] = 0 \tag{A53}$$

A.3.3. $D\delta w^{\mathrm{a}}[\Delta \ddot{p}^{\mathrm{a}}]$.

$$\begin{aligned} D\delta w_1^{\mathrm{a}}[\Delta \ddot{p}^{\mathrm{a}}] = {} & \beta\Delta t^2 \int_{B^{\mathrm{s}}} \delta p^{\mathrm{a}} n \left(-2\frac{1}{\Theta\overline{R}} c - \rho^{\mathrm{aR}} \overline{c}\right) \dot{p}^{\mathrm{a}} \Delta \ddot{p}^{\mathrm{a}} dv \\ & + \gamma\Delta t \int_{B^{\mathrm{s}}} \delta p^{\mathrm{a}} n \left\{\frac{(1-s^{\mathrm{w}})}{\Theta\overline{R}} - \rho^{\mathrm{aR}} c\right\} \Delta \ddot{p}^{\mathrm{a}} dv \end{aligned} \tag{A54}$$

$$D\delta w_2^{\mathrm{a}}[\Delta \ddot{p}^{\mathrm{a}}] = \beta\Delta t^2 \int_{B^{\mathrm{s}}} \delta p^{\mathrm{a}} n \left(\frac{1}{\Theta\overline{R}} c + \rho^{\mathrm{aR}} \overline{c}\right) \dot{p}^{\mathrm{w}} \Delta \ddot{p}^{\mathrm{a}} dv \tag{A55}$$

$$D\delta w_3^{\mathrm{a}}[\Delta \ddot{p}^{\mathrm{a}}] = \beta\Delta t^2 \int_{B^{\mathrm{s}}} \delta p^{\mathrm{a}} \left\{-c\rho^{\mathrm{aR}} + \frac{(1-s^{\mathrm{w}})}{\Theta\overline{R}}\right\} \mathrm{div}\, \boldsymbol{v}^{\mathrm{s}} \Delta \ddot{p}^{\mathrm{a}} dv \tag{A56}$$

$$D\delta w_4^{\mathrm{a}}[\Delta \ddot{p}^{\mathrm{a}}] = \frac{1}{g}\beta\Delta t^2 \int_{B^{\mathrm{s}}} \mathrm{grad}\, \delta p^{\mathrm{a}} \cdot \left(\;\mathrm{grad}\, p^{\mathrm{a}} \overline{k}_{\mathrm{p}}^{\mathrm{as}} \Delta \ddot{p}^{\mathrm{a}} + \;\mathrm{grad}\, \Delta \ddot{p}^{\mathrm{a}} k^{\mathrm{as}}\right) dv \tag{A57}$$

$$D\delta w_5^{\mathrm{a}}[\Delta \ddot{p}^{\mathrm{a}}] = -\frac{1}{g}\beta\Delta t^2 \int_{B^{\mathrm{s}}} \mathrm{grad}\, \delta p^{\mathrm{a}} \cdot \boldsymbol{b} \left(\overline{k}_{\mathrm{p}}^{\mathrm{as}} \rho^{\mathrm{aR}} + k^{\mathrm{as}} \frac{1}{\Theta\overline{R}}\right) \Delta \ddot{p}^{\mathrm{a}} dv \tag{A58}$$

$$D\delta w_6^{\mathrm{a}}[\Delta \ddot{p}^{\mathrm{a}}] = \frac{1}{g}\beta\Delta t^2 \int_{B^{\mathrm{s}}} \mathrm{grad}\, \delta p^{\mathrm{a}} \cdot \boldsymbol{a}^{\mathrm{s}} \left(\overline{k}_{\mathrm{p}}^{\mathrm{as}} \rho^{\mathrm{aR}} + k^{\mathrm{as}} \frac{1}{\Theta\overline{R}}\right) \Delta \ddot{p}^{\mathrm{a}} dv \tag{A59}$$

$$D\delta w_7^{\mathrm{a}}[\Delta \ddot{p}^{\mathrm{a}}] = 0 \tag{A60}$$

APPENDIX: LIST OF NOTATIONS

a_{lg}	material parameter of LG model
$\boldsymbol{a}^{\mathrm{a}}$	acceleration of pore air
$\boldsymbol{a}^{\mathrm{s}}$	acceleration of solid skeleton
$\Delta\boldsymbol{a}^{\mathrm{s}}$	variation of $\boldsymbol{a}^{\mathrm{s}}$ in Newton-Raphson method
$\boldsymbol{a}^{\mathrm{w}}$	acceleration of pore water
b_{lg}	material parameter of LG model
$\boldsymbol{b}$	body force vector
$\boldsymbol{b}^{\mathrm{s}}$	left Cauchy-Green tensor of solid skeleton

$\boldsymbol{b}^{\alpha}$	body force vector of phase α
B	Biot coefficient
B^{s}	simple body in the current configuration of solid skeleton
∂B^{s}	boundary of a simple body in the current configuration of solid skeleton
c	specific moisture capacity
c_{lg}	material parameter of LG model
$\overline{c}$	derivative of specific soil moisture c with respect to suction p^{c}
$\boldsymbol{c}$	fourth-order spatial elasticity tensor in the current configuration
$\boldsymbol{d}^{\mathrm{s}}$	deformation rate tensor of solid skeleton
e	void ratio
e_0	initial void ratio
E	normalized void ratio
$\boldsymbol{F}^{\mathrm{s}}$	deformation gradient of solid skeleton
g	gravity acceleration
g'	finite strain coefficient of consolidation
$\boldsymbol{I}$	second-order identity tensor (Kronecker delta function)
$\mathcal{I}$	fourth-order identity tensor
J^{s}	Jacobian of solid skeleton
k^{as}	permeability coefficients of pore air
$k_{\mathrm{r}}^{\mathrm{as}}$	relative permeability coefficient of air
$k_{\mathrm{s}}^{\mathrm{as}}$	maximum coefficient of air permeability
k^{ws}	permeability coefficients of pore water
$k_{\mathrm{r}}^{\mathrm{ws}}$	relative permeability coefficient of water
$k_{\mathrm{s}}^{\mathrm{ws}}$	maximum coefficient of water permeability
$\overline{k}_{\mathrm{p}}^{\mathrm{as}}$	derivative of pore air permeability k^{as} with respect to suction p^{c}
$\overline{k}_{\mathrm{p}}^{\mathrm{ws}}$	derivative of pore water permeability k^{ws} with respect to suction p^{c}
K^{w}	bulk modulus of pore water
ℓ	height of solid layer
n	porosity in the current configuration
n^{a}	volume fraction of pore air in the current configuration
n^{s}	volume fraction of solid skeleton in the current configuration
n^{w}	volume fraction of pore water in the current configuration
n^{α}	volume fraction of a phase α in the current configuration
n_{vg}	material parameter of VG model
N_n^{f}	bilinear interpolation function for pore water and pore air pressures
N_n^{s}	eight-node serendipity interpolation function for displacement of solid skeleton
m_{vg}	material parameter of VG model
p^{a}	pore air pressure
$\dot{p}^{\mathrm{a}}$	material time derivative of pore air pressure with respect to solid skeleton
$\ddot{p}^{\mathrm{a}}$	second material time derivative of pore air pressure with respect to solid skeleton
$\Delta\ddot{p}^{\mathrm{a}}$	variation of $\ddot{p}^{\mathrm{a}}$ in Newton-Raphson method
p_e^{a}	approximated pore air pressure in the element
p_n^{a}	pore air pressure at the four corner nodes n
p^{c}	suction stress or capillary pressure
p^{w}	pore water pressure
$\dot{p}^{\mathrm{w}}$	material time derivative of pore water pressure with respect to solid skeleton
$\ddot{p}^{\mathrm{w}}$	second material time derivative of pore water pressure with respect to solid skeleton
$\Delta\ddot{p}^{\mathrm{w}}$	variation of $\ddot{p}^{\mathrm{w}}$ in Newton-Raphson method
p_e^{w}	approximated pore water pressure in the element
p_n^{w}	pore water pressure at the four corner nodes n
$\overline{p}$	mean pore pressure
$\overline{p}^{\mathrm{a}}$	prescribed pore air pressure at $\partial B_{\mathrm{ap}}^{\mathrm{s}}$
$\overline{p}^{\mathrm{w}}$	prescribed pore water pressure at $\partial B_{\mathrm{wp}}^{\mathrm{s}}$

Int. J. Numer. Anal. Meth. Geomech. 2012; **36**:1535–1573
DOI: 10.1002/nag

p^{α}	interaction force vector between phase α and other phases
$\overline{q}^{a}$	prescribed mass flux of pore air on a unit area with unit normal vector n at ∂B^{s}_{aq}
$\overline{q}^{w}$	prescribed mass flux of pore water on a unit area with unit normal vector n at ∂B^{s}_{wq}
$\overline{R}$	specific gas constant of air
s^{a}	degree of air saturation in the current configuration
s^{a}_{r}	residual (minimum) degree of air saturation
s^{w}	degree of water saturation in the current configuration
s^{w}_{e}	effective degree of water saturation
s^{w}_{r}	residual (minimum) degree of water saturation
s^{w}_{s}	maximum degree of water saturation
$\overline{\boldsymbol{t}}$	prescribed traction vector at ∂B^{s}_{t}
T	dimensionless time factor
Δt	time increment
$\boldsymbol{u}^{as}$	relative displacement of pore air to solid skeleton
$\boldsymbol{u}^{ws}$	relative displacement of pore water to solid skeleton
$\boldsymbol{u}^{s}$	displacement of solid skeleton
$\boldsymbol{u}^{s}_{e}$	approximated displacement of solid skeleton in the element
$\boldsymbol{u}^{s}_{n}$	displacement of solid skeleton at the eight nodes n
$\boldsymbol{u}^{\alpha}$	displacement of the material point X^{α}
$\boldsymbol{u}^{s}$	prescribed displacement vector of solid skeleton at ∂B^{s}_{u}
$\boldsymbol{v}^{as}$	relative velocity of pore air to solid skeleton
$\boldsymbol{v}^{ws}$	relative velocity of pore water to solid skeleton
$\boldsymbol{v}^{s}$	velocity of solid skeleton
$\boldsymbol{v}^{\alpha}$	velocity of the material point X^{α}
$\boldsymbol{x}$	spatial description of the material point X^{α}
z	material coordinate of solid skeleton
Z	dimensionless vertical material coordinate
α_{vg}	material parameter of VG model
α_{vis}	material parameter reflecting the viscous damping characteristics of solid skeleton
β	numerical parameter of Newmark time integration scheme
γ	numerical parameter of Newmark time integration scheme
η_{lg}	material parameter of LG model
η_{vg}	material parameter of VG model
Θ	absolute temperature
$\boldsymbol{\mu}^{\alpha}$	material parameter tensor
λ	Lamé constant of neo-Hookean model
μ	Lamé constant of neo-Hookean model
ξ_{lg}	material parameter of LG model
ξ_{vg}	material parameter of VG model
ρ	overall density of mixture in the current configuration
ρ^{aR}	intrinsic density of pore air
ρ^{sR}	intrinsic density of solid skeleton
ρ^{wR}	intrinsic density of pore water
$\boldsymbol{\sigma}'_{y}$	vertical Cauchy effective stress
$\boldsymbol{\sigma}$	total Cauchy stress tensor
$\boldsymbol{\sigma}'$	Cauchy effective stress tensor
$\boldsymbol{\sigma}'_{inv}$	inviscid part of $\boldsymbol{\sigma}'$
$\boldsymbol{\sigma}'_{vis}$	viscous part of $\boldsymbol{\sigma}'$
$\boldsymbol{\sigma}^{a}$	averaged Cauchy stress tensor for pore air
$\boldsymbol{\sigma}^{s}$	averaged Cauchy stress tensor for solid skeleton
$\boldsymbol{\sigma}^{w}$	averaged Cauchy stress tensor for pore water
$\boldsymbol{\sigma}^{\alpha}$	averaged Cauchy stress tensor of phase α
χ	Bishop parameter

ACKNOWLEDGEMENTS

This study is financially supported by JSPS, Japan Society for the Promotion of Science, for Grants-in-Aid for Scientific Research under Contract No. 17560441 and the Ministry of Education, Culture, Sports, Science and Technology of Japan (MEXT). The authors thank Mr. Akiyoshi Kamura, a former graduate student of Tohoku University, for his cooperation in numerical analyses. The second author acknowledges support from National Science Foundation under Grant Numbers CMMI-0824440 and CMMI-0936421.

REFERENCES

1. Biot MA. Theory of finite deformations of porous solids. *Indiana University Mathematics Journal* 1972; **21**(7): 597–620.
2. Carter JP, Booker JR, Small JC. The analysis of finite elasto-plastic consolidation. *International Journal for Numerical and Analytical Methods in Geomechanics* 1979; **3**:107–129.
3. Yatomi C, Yashima A, Iizuka A, Sano I. General theory of shear bands formation by a non-coaxial Cam-clay model. *Soils and Foundations* 1989; **29**(3):41–53.
4. Borja RI, Alarcón E. A mathematical framework for finite strain elastoplastic consolidation. Part 1: Balance laws, variational formulation, and linearization. *Computer Methods in Applied Mechanics and Engineering* 1995; **122**:145–171.
5. Borja RI, Tamagnini C, Alarcón, E. Finite strain elastoplastic consolidation, Part 2: Finite element implementation and numerical examples. *Computer Methods in Applied Mechanics and Engineering* 1998; **159**:103–122.
6. Armero F. Formulation and finite element implementation of a multiplicative model of coupled poro-plasticity at finite strains under fully saturated conditions. *Computer Methods in Applied Mechanics and Engineering* 1999; **171**:205–241.
7. Larsson J, Larsson R. Non-linear analysis of nearly saturated porous media: theoretical and numerical formulation. *Computer Methods in Applied Mechanics and Engineering* 2002; **191**:3885–3907.
8. Li C, Borja RI, Regueiro RA. Dynamics of porous media at finite strain. *Computer Methods in Applied Mechanics and Engineering* 2004; **193**:3837–3870.
9. Biot MA. Mechanics of deformation and acoustic propagation in porous media. *Journal of Applied Physics* 1962; **33**(4):1482–1498.
10. Zienkiewicz OC. Chang CT, Hinton E. Non-linear seismic response and liquefaction. *International Journal for Numerical and Analytical Methods in Geomechanics* 1978; **2**:381–404.
11. Ghaboussi J, Dikmen SU. Liquefaction Analysis of Horizontally Layered Sands. *Journal of the Geotechnical Engineering Division, ASCE* 1978; **104**(3):341–356.
12. Ishihara K, Towhata I. Effective stress method in one-dimensional soil response analysis. *Proceedings of the 7th World Conference of Earthquake Engineering*, vol. **3**, 1980; 73–80.
13. Zienkiewicz OC, Shiomi T. Dynamic behavior of saturated porous media: The generalized Biot formulation and its numerical solution. *International Journal for Numerical and Analytical Method in Geomechanics* 1984; **8**: 71–96.
14. Prevost HJ. A simple plasticity theory for frictional cohesionless soils. *Soil Dynamics and Earthquake Engineering* 1985; **4**:28–36.
15. Finn WDL, Yogendrakumar M, Yoshida N, Yoshida H. *TARA-3: A program to compute the response of 2-D embankments and soil-structure interaction systems to seismic loadings*. Department of Civil Engineering, University of British Columbia: Vancouver, Canada, 1986.
16. Iai S, Kameoka T. Finite element analysis of earthquake induced damage to anchored sheet pile quay walls. *Soils and Foundations* 1993; **33**(1):71–91.
17. Oka F, Yashima A, Shibata T, Kato M, Uzuoka R. FEM-FDM coupled liquefaction analysis of a porous soil using an elasto-plastic model. *Applied Scientific Research* 1994; **52**:209–245.
18. Fukutake K, Ohtsuki A. Three-dimensional liquefaction analysis of partially improved ground. *Proceedings of the 1st Int. Conf. on Earthquake Geotechnical Engineering*, Tokyo, 1995; 851–856.
19. Fujii S, Isemoto N, Satou Y, Kaneko O, Funahara H, Arai T, Tokimatsu K. Investigation and analysis of a pile foundation damaged by liquefaction during the 1995 Hyogoken-Nambu earthquake. *Soils and Foundations*, Special Issue on Geotechnical Aspects of the January 17 1995 Hyogoken-Nambu Earthquake 1998; **2**:179–192.
20. Yoshida N, Finn WDL. Simulation of liquefaction beneath an impermeable surface layer. *Soil Dynamics and Earthquake Engineering* 2000; **19**:333–338.
21. Elgamal A, Yang Z, Parra E. Computational modeling of cyclic mobility and post-liquefaction site response. *Soil Dynamics and Earthquake Engineering* 2002; **22**:259–271.
22. Popescu R, Prevost JH, Deodatis G, Chakrabortty P. Dynamics of nonlinear porous media with applications to soil liquefaction. *Soil Dynamics and Earthquake Engineering* 2006; **26**:648–665.
23. Taiebat M, Shahir H, Pak A. Study of pore pressure variation during liquefaction using two constitutive models for sand. *Soil Dynamics and Earthquake Engineering* 2007; **27**:60–72.
24. Jeremic B, Cheng Z, Taiebat M, Dafalias Y. Numerical simulation of fully saturated porous materials. *International Journal for Numerical and Analytical Method in Geomechanics* 2008; **32**:1635–1660.

25. Peng J, Lu J, Law KH, Elgamal A. ParCYCLIC: Finite element modeling of earthquake liquefaction response on parallel computers. *International Journal for Numerical and Analytical Method in Geomechanics* 2004; **28**: 1207–1232.
26. Uzuoka R, Sento N, Kazama M, Zhang F, Yashima A, Oka F. Three-dimensional numerical simulation of earthquake damage to group-piles in a liquefied ground. *Soil Dynamics and Earthquake Engineering* 2007; **27**:395–413.
27. Lu CW, Oka F, Zhang F. Analysis of soil-pile-structure interaction in a two-layer ground during earthquakes considering liquefaction. *International Journal for Numerical and Analytical Method in Geomechanics* 2008; **32**:863–895.
28. Cubrinovski M, Uzuoka R, Sugita H, Tokimatsu K, Sato M, Ishihara K, Tsukamoto Y, Kamata T. Prediction of pile response to lateral spreading by 3-D soil-water coupled dynamic analysis: Shaking in the direction of ground flow. *Soil Dynamics and Earthquake Engineering* 2008; **28**:421–435.
29. Uzuoka R, Cubrinovski M, Sugita H, Sato M, Tokimatsu K, Sento N, Kazama M, Zhang F, Yashima A, Oka F. Prediction of pile response to lateral spreading by 3-D soil-water coupled dynamic analysis: Shaking in the direction perpendicular to ground flow. *Soil Dynamics and Earthquake Engineering* 2008; **28**:436–452.
30. Elgamal A, Lu J, Forcellini D. Mitigation of liquefaction-induced lateral deformation in a sloping stratum: Three-dimensional numerical simulation. *Journal of Geotechnical and Geoenvironmental Engineering* 2009; **135**(11): 1672–1682.
31. Meroi EA, Schrefler BA, Zienkiewicz OC. Large strain static and dynamic semi-saturated solid behavior. *International Journal for Numerical and Analytical Methods in Geomechanics* 1995; **19**:81–106.
32. Uzuoka R, Kubo T, Yashima A, Zhang F. Liquefaction analysis with seepage to partially saturated surface soil. *Journal of Geotechnical Engineering, Japan Society of Civil Engineers* 2001; **694**(III-57):153–163. (in Japanese)
33. Kazama M, Takamura H, Unno T, Sento N, Uzuoka R. Liquefaction mechanism of unsaturated volcanic sandy soils. *Journal of Geotechnical Engineering, Japan Society of Civil Engineers* 2006; **62**(2):546–561. (in Japanese).
34. Schrefler BA, Scotta R. A fully coupled dynamic model for two-phase fluid flow in deformable porous media. *Computer Methods in Applied Mechanics and Engineering* 2001; **190**:3223–3246.
35. Ravichandran N. Fully coupled finite element model for dynamics of partially saturated soils. *Soil Dynamics and Earthquake Engineering* 2009; **29**:1294–1304.
36. Ravichandran N, Muraleetharan KK. Dynamics of unsaturated soils using various finite element formulations. *International Journal for Numerical and Analytical Methods in Geomechanics* 2009; **33**:611–631.
37. Borja RI. On the mechanical energy and effective stress in saturated and unsaturated porous continua. *International Journal of Solids and Structures* 2006; **43**(6):1764–1786.
38. Borja RI, Koliji A. On the effective stress in unsaturated porous continua with double porosity. *Journal of the Mechanics and Physics of Solids* 2009; **57**(8):1182–1193.
39. de Boer R. Contemporary progress in porous media theory. *Applied Mechanics Reviews* 2000; **53**(12):323–369.
40. Schrefler BA. Mechanics and thermodynamics of saturated/unsaturated porous materials and quantitative solutions. *Applied Mechanics Reviews* 2002; **55**(4):351–388.
41. Grozic JLH, Imam SMR, Robertson PK, Morgenstern NR. Constitutive modeling of gassy sand behaviour. *Canadian Geotechnical Journal* 2005; **42**:812–829.
42. Mehrabadi AJ, Abdi MA, Popescu R. Analysis of liquefaction susceptibility of nearly saturated sands. *International Journal for Numerical and Analytical Methods in Geomechanics* 2007; **31**:691–714.
43. Mason EA, Monchick L. Survey of the equations of state and transport properties of moist gases. In *Humidity and Moisture: Measurement and Control in Science and Industry*, Vol. **3**, Wexler A (ed.). Reinhold Pub. Corp.: New York, 1965; 257–272.
44. Hassanizadeh M, Gray WG. General conservation equations for multi-phase systems: 3. Constitutive theory for porous media flow mass. *Advances in Water Resources* 1980; **3**:25–40.
45. Hassanizadeh M, Gray WG. Mechanics and thermodynamics of multiphase flow in porous media including interphase boundaries. *Advances in Water Resources* 1990; **13**:169–186.
46. Ehlers W. Constitutive equations for granular materials in geomechanical context. In *Continuum Mechanics in Environmental Sciences and Geophysics*, CISM Courses and Lectures **337**, Hutter K (ed.). Springer-Verlag: New York, 1993; 313–402.
47. Houlsby GT. The work input to an unsaturated granular material. *Geotechnique* 1997; **47**(1):193–196.
48. Muraleetharan KK, Wei C. Dynamic behaviour of unsaturated porous media: governing equations using the Theory of Mixtures with Interfaces (TMI). *International Journal for Numerical and Analytical Methods in Geomechanics* 1999; **23**:1579–1608.
49. Borja RI. Cam-Clay plasticity. Part V: A mathematical framework for three-phase deformation and strain localization analyses of partially saturated porous media. *Computer Methods in Applied Mechanics and Engineering* 2004; **193**:5301–5228.
50. Li XS. Thermodynamics-based constitutive framework for unsaturated soils. 1: Theory. *Geotechnique* 2007; **57**(5): 411–422.
51. Bishop AW, Blight GE. Some aspects of effective stress in saturated and partly saturated soils. *Geotechnique* 1966; **13**(3):177–197.
52. Terzaghi K. *Die Berechnung der Durchlässigkeitziffer des Tones aus dem Verlauf der hydrodynamischen Spannungserscheinungen, Theory to Practice in Soil Mechanics*. John Wiley & Sons: New York, 1923.
53. van Genuchten MT. A closed-form equation for predicting the hydraulic conductivity of unsaturated soils. *Soil Science Society of America Journal* 1980; **44**:892–898.

DOI: 10.1002/nag

54. McKee CR, Bumb AC. Flow-Testing Coalbed Methane Production Wells in the Presence of Water and Gas. *SPE Formation Evaluation* 1987; **2**(4):599–608.
55. Carsel RF, Parrish RS. Developing Joint Probability Distributions of Soil Water Retention Characteristics. *Water Resources Research* 1988; **24**(5):755–769.
56. Bonet J, Wood RD. *Nonlinear continuum mechanics for finite element analysis*. Cambridge University Press: England, 1997; 119–125.
57. Simo JC, Hughes TJR. *Computational Inelasticity*. Springer: New York, 1998.
58. Simo JC. Algorithms for static and dynamic multiplicative plasticity that preserve the classical return mapping schemes of the infinitesimal theory. *Computer Methods in Applied Mechanics and Engineering* 1992; **99**:61–112.
59. Holzapfel GA. *Nonlinear solid mechanics: A continuum approach for engineering*. John Wiley & Sons Ltd.: New York, 2000.
60. Zienkiewicz OC, Taylor RL. *The Finite Element Method*, Fourth edition, Vol. **2**. McGraw-Hill: New York, 1991.
61. Hughes TJR. *The Finite Element Method, Linear Static and Dynamic Finite Element Analysis*. Dover Publications, Inc.: New York, 2000.
62. Gibson RE, Englund GL, Hussey MJL. The theory of one-dimensional consolidation of saturated clays. I. Finite nonlinear consolidation of thin homogeneous layers. *Geotechnique* 1967; **17**(3):261–273.
63. Gibson RE, Schiffman RL, Cargill KW. The theory of one-dimensional consolidation of saturated clays. II. Finite nonlinear consolidation of thick homogeneous layers. *Canadian Geotechnical Journal* 1981; **18**(2):280–293.
64. Morris PH. Analytical solutions of linear finite-strain one-dimensional consolidation. *Journal of Geotechnical and Geo environmental Engineering, ASCE* 2002; **128**(4):319–326.
65. Xie KH, Leo CJ. Analytical solutions of one-dimensional large strain consolidation of saturated and homogeneous clays. *Computers and Geotechnics* 2004; **31**:301–314.
66. Liakopoulos A. Transient flow through unsaturated porous media. *PhD thesis*, University of California at Berkeley, 1964.
67. Lewis RW, Schrefler BA. *The Finite Element Method in the Static and Dynamic Deformation and Consolidation of Porous Media*, Second edition. John Wiley & Sons Ltd.: New York, 1998.
68. Zienkiewicz OC, Chan AHC, Pastor M, Schrefler BA, Shiomi T. *Computational Geomechanics with Special Reference to Earthquake Engineering*. John Wiley & Sons Ltd.: New York, 1999.
69. Ehlers W, Graf T, Ammann M. Deformation and localization analysis of partially saturated soil. *Computer Methods in Applied Mechanics and Engineering* 2004; **193**:2285–2910.
70. White JA, Borja RI. Stabilized low-order finite elements for coupled solid-deformation/fluid-diffusion and their application to fault zone transients. *Computer Methods in Applied Mechanics and Engineering* 2008; **197**: 4353–4366.

DOI: 10.1002/nag